UNIVERSIDAD DE INVESTIGACIÓN DE TECNOLOGÍA EXPERIMENTAL YACHAY

Escuela de Ciencias Ciencias Físicas y Nanotecnología

TÍTULO: Photoactive activity of different natural dyes for possible applications in solar cells.

Trabajo de integración curricular presentado como requisito para la obtención del título de Ingeniero en Nanotecnología

Autor:

Romero Proaño Pablo Andrés

Tutor:

Ph.D. Bramer Escamilla Werner

Urcuquí, septiembre 2021

SECRETARÍA GENERAL
(Vicerrectorado Académico/Cancillería)
ESCUELA DE CIENCIAS FÍSICAS Y NANOTECNOLOGÍA
CARRERA DE NANOTECNOLOGÍA
ACTA DE DEFENSA No. UITEY-PHY-2021-00020-AD

A los 23 días del mes de septiembre de 2021, a las 15:00 horas, de manera virtual mediante videoconferencia, y ante el Tribunal Calificador, integrado por los docentes:

Presidente Tribunal de Defensa	Dr. REINOSO CARLOS , Ph.D.
Miembro No Tutor	Dr. CHACON TORRES, JULIO CESAR , Ph.D.
Tutor	Dr. BRAMER ESCAMILLA , WERNER , Ph.D.

El(la) señor(ita) estudiante **ROMERO PROAÑO, PABLO ANDRES**, con cédula de identidad No. **1004180251**, de la **ESCUELA DE CIENCIAS FÍSICAS Y NANOTECNOLOGÍA**, de la Carrera de **NANOTECNOLOGÍA**, aprobada por el Consejo de Educación Superior (CES), mediante Resolución **RPC-SO-13-No.156-2015**, realiza a través de videoconferencia, la sustentación de su trabajo de titulación denominado: **Photoactive activity of different natural dyes for possible applications in solar cells.** , previa a la obtención del título de **INGENIERO/A EN NANOTECNOLOGÍA**.

El citado trabajo de titulación, fue debidamente aprobado por el(los) docente(s):

Tutor	Dr. BRAMER ESCAMILLA , WERNER , Ph.D.

Y recibió las observaciones de los otros miembros del Tribunal Calificador, las mismas que han sido incorporadas por el(la) estudiante.

Previamente cumplidos los requisitos legales y reglamentarios, el trabajo de titulación fue sustentado por el(la) estudiante y examinado por los miembros del Tribunal Calificador. Escuchada la sustentación del trabajo de titulación a través de videoconferencia, que integró la exposición de el(la) estudiante sobre el contenido de la misma y las preguntas formuladas por los miembros del Tribunal, se califica la sustentación del trabajo de titulación con las siguientes calificaciones:

Tipo	Docente	Calificación
Presidente Tribunal De Defensa	Dr. REINOSO CARLOS , Ph.D.	9,7
Tutor	Dr. BRAMER ESCAMILLA , WERNER , Ph.D.	10,0
Miembro Tribunal De Defensa	Dr. CHACON TORRES, JULIO CESAR , Ph.D.	9,8

Lo que da un promedio de: **9.8 (Nueve punto Ocho)**, sobre 10 (diez), equivalente a: **APROBADO**

Para constancia de lo actuado, firman los miembros del Tribunal Calificador, el/la estudiante y el/la secretario ad-hoc.

Certifico que *en cumplimiento del Decreto Ejecutivo 1017 de 16 de marzo de 2020, la defensa de trabajo de titulación (o examen de grado modalidad teórico práctica) se realizó vía virtual, por lo que las firmas de los miembros del Tribunal de Defensa de Grado, constan en forma digital.*

ROMERO PROAÑO, PABLO ANDRES
Estudiante

Firmado electrónicamente por:
CARLOS ALBERTO
REINOSO JEREZ

Dr. REINOSO CARLOS , Ph.D.
Presidente Tribunal de Defensa

WERNER BRAMER ESCAMILLA
Firmado digitalmente por WERNER BRAMER ESCAMILLA
Fecha: 2021.09.23 21:29:21 -05'00'

Dr. BRAMER ESCAMILLA , WERNER , Ph.D.
Tutor

Dr. CHACON TORRES, JULIO CESAR , Ph.D.
Miembro No Tutor

CIFUENTES TAFUR, EVELYN CAROLINA
Secretario Ad-hoc

AUTORÍA

Yo, **Pablo Andrés Romero Proaño**, con cédula de identidad 1004180251, declaro que las ideas, juicios, valoraciones, interpretaciones, consultas bibliográficas, definiciones y conceptualizaciones expuestas en el presente trabajo; así cómo, los procedimientos y herramientas utilizadas en la investigación, son de absoluta responsabilidad de el/la autora (a) del trabajo de integración curricular, ensayo o artículo científico. Así mismo, me acojo a los reglamentos internos de la Universidad de Investigación de Tecnología Experimental Yachay.

Urcuquí, septiembre 2021.

_____

Pablo Andrés Romero Proaño
CI: 1004180251

AUTORIZACIÓN DE PUBLICACIÓN

Yo, **Pablo Andrés Romero Proaño,** con cédula de identidad 1004180251, cedo a la Universidad de Tecnología Experimental Yachay, los derechos de publicación de la presente obra, sin que deba haber un reconocimiento económico por este concepto.

Asimismo, autorizo a la Universidad que realice la digitalización y publicación de este trabajo de integración curricular, en el repositorio virtual, de conformidad a lo dispuesto en el Art. 144 de la Ley Orgánica de Educación Superior.

Urcuquí, septiembre 2021.

_____
Pablo Andrés Romero Proaño
CI: 1004180251

Acknowledgements

Resumen

En este trabajo, se utilizaron tintes naturales extraídos de mortiño y flor de Jamaica originarios de la sierra andina de Ecuador como tintes sensibilizadores en celdas solares sensibilizadas por colorantes (DSSC). Además, se utilizaron nanotubos de carbono de pared simple (SWCNTs) y películas de hollín de vela como contraelectrodos. Las propiedades ópticas de los colorantes obtenidos de un proceso de extracción simple usando etanol como solvente fueron investigadas usando espectroscopía UV-Vis. La estructura de la película de dióxido de titanio (TiO_2) en el fotoanodo y la película de SWCNTs en el contraelectrodo se caracterizaron usando difracción de rayos X (XRD) y espectroscopía Raman. Se encontró que el proceso de deposición de la película de SWCNTs, que implica un recubrimiento de gel utilizando polietilenglicol (PEG) como aglutinante, no introduce defectos en la estructura cristalina de los SWCNTs. El rendimiento fotovoltaico de las celdas fabricadas se evaluó a partir de sus curvas I-V y parámetros fotovoltaicos como potencia máxima de salida (P_{max}), factor de llenado (FF) y eficiencia de conversión de energía (η). Las DSSCs que usaban la película de SWCNTs como contraelectrodo exhibieron los valores más altos de P_{max}, FF y η debido a una baja resistencia a la transferencia de carga y una mejor actividad electrocatalítica en comparación a las celdas que usaban la pelicula de hoolín de vela. Finalmente, se estudió el efecto del tiempo de sensibilización de la película TiO_2 en los tintes naturales. Al aumentar el tiempo de sensibilización a 20 horas, se mejora la respuesta espectral del fotoanodo a la luz visible con un incremento de η por un factor de 2.65.

Palabras clave: Sensibilizador, celdas solares sensibilizadas por colorantes, nanotubos de carbono, fotoánodo, rendimiento fotovoltaico.

Abstract

In this work, natural dyes extracted from mortiño and Jamaica flower originally from the Andean sierra of Ecuador were used as dye sensitizers in dye-sensitized solar cells (DSSCs). In addition, two kind of counter electrodes were used, SWCNTs and candle soot films on fluorine-doped tin oxide (FTO) coated glass. The optical properties of the dyes obtained from a simple extraction process using ethanol as solvent were investigated using UV-Vis spectroscopy. The structure of the titanium dioxide (TiO_2) film at the photoanode and the SWCNTs film at the counter electrode were characterized using X-ray powder diffraction (XRD) and Raman spectroscopy. It was found that the film deposition process of SWCNTs, involving a gel coating using polyethylene glycol (PEG) as binder, does not introduce defects in the crystalline structure of the SWCNTs. The photovoltaic performance of the fabricated cells evaluated from their I-V curves and photovoltaic parameters as maximum power output (P_{max}), fill factor (FF) and power conversion efficiency (η). The DSSCs using the SWCNTs film as counter electrode exhibited the highest P_{max}, FF, and η values due to a low charge transfer resistance and better electrocatalytic activity in comparison with the cells using candle soot. Finally, the effect of the sensitization time of the TiO_2 film on natural dyes is studied. By increasing the sensitization time to 20 hours, the spectral response of TiO_2 to visible light with and increase of η by a factor of 2.65.

Keywords: Sensitizer, dye-sensitized solar cells, SWCNTs, photoanode, photovoltaic performance.

Contents

List of Figures

List of Tables

Chapter 1

Introduction

1.1 Photovoltaic cells

A photovoltaic cell (PV) or solar cell is a device that uses the photoelectric effect to convert the energy of the light directly into electricity. This technology harnesses solar power, and it is considered the most promising of renewable energy technologies. In 1905, Albert Einstein described how photon absorption causes the release of charged particles from or within a material, for which he received the Nobel Prize in Physics in 1921.[1,2]

Three generations of solar cells have been the most studied up to now. The first generation is conformed by monocrystalline and polycrystalline silicon solar cells. These cells use a p-n junction by doping silicon with other elements[3] and can achieve a power conversion efficiency (PCE) around $\sim 25\%$.[1] The second generation is known as thin-film solar cells and is formed by compound films such as cadmium telluride (CdTe), gallium arsenide (GaAs), copper indium gallium selenide (CIGS), among others.[4] The third generation refers to hybrid film solar cells and is considered as emerging PV. This new generation includes dye-sensitized solar cells (highest PCE ≈ 14 %)[5], organic/polymer solar cells, quantum dots solar cells, perovskite solar cells, among others.[3] This last generation has low processing costs and minor elemental impact, which subjects them to intensive research and development.[4]

1.2 Dye sensitized solar cells

Dye-sensitized solar cells (DSSC) belong to the third-generation of PV cells, and their conversion of visible light into electricity is based on a wide bandgap semiconductor sensitization.[6] In 1990, Grätzel and his
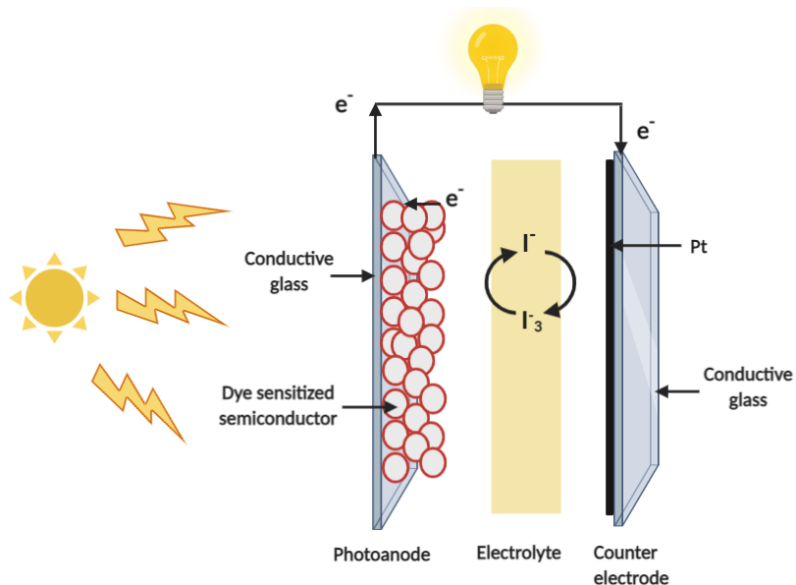
Figure 1.1: Schematic structure of a conventional DSSC formed by a photoanode with a sensitized semiconductor layer over transparent conductive glass (TCO), an electrolyte, and a counter electrode with a catalyst film deposited over TCO.

co-workers developed the DSSC or Grätzel cell.[7] In a DSSC, the photoreceptor and charge carrier are present in different components of the cell, contrary to conventional solar cells using a p-n junction. This process assembles photosynthesis, where chlorophyll absorbs photons but does not transfer the charge.[3]

1.2.1   Structure and components of a DSSC

Before talking about the operation principle of a DSSC, it is essential to understand the role of each component present in this cell. Figure 1.1 illustrates the structure of a DSSC, which present five main components: a conducting glass substrate, a wide bandgap semiconductor (usually a nanocrystalline TiO_2 film), a dye sensitizer anchored on to the surface of the semiconductor, an electrolyte solution inserted between the electrodes and a counter electrode.[8]

The transparent conducting glass is typically made of coating glass with a layer of transparent conducting oxide (TCO) as indium tin oxide (ITO), fluorine-doped tin oxide (FTO), or aluminum-doped zinc oxide (AZO).[9] This conductive glass acts as a current collector and a gateway for the light; for this reason, the overall performance of DSSCs depends, up to a point, on this substrate conductivity and transmittance.[10]

The wide bandgap semiconductor corresponds to a mesoporous metal oxide layer, which forms the photoanode in the DSSC. The photoanode acts as an electron collector and the material from which it is made must present a homogeneous nano-micro structure that ensures the maximum surface area in which the dye is absorbed. Other requirements of the photoanode material are: small interfacial electron recombination with fast electron transport to ensure the appropriate distance of electron diffusion, the contact between photoanode and electrolyte, and prevent the material degradation from photo corrosion.[11] Then, the power conversion efficiency of the cell strongly depends on the surface area, morphology, porosity, crystallinity, and the conduction band of the semiconductor. It is important to mention that the most common photoanode material used in DSSCs is TiO_2 and different nanocomposites with TiO_2.[10,12]

A dye sensitizer is anchored onto the surface of the metal oxide semiconductor through a covalent bond and harvest incident sunlight. After absorbing sunlight, the dye is photoexcited and injects an electron into the metal oxide semiconductor.[6] There are three main classes of photosensitizers: Ruthenium(II) polypyridyl complexes, Zn-porphyrin derivatives and Metal-free organic dyes. .[10]

The electrolyte inserted between the electrodes is usually an organic solvent containing the redox couple, such as iodide/triiodide couple. It is in charge of regenerating the oxidized dye and the electrolyte itself during operation. Finally, the counter electrode (cathode) consists of a thin film catalyst deposition onto the TCO and performs three functions: catalyze the redox reaction of the electrolyte, act as positive electrode of primary cells to collect the electrons from the external circuit, and reflect the unabsorbed light from the back of the cell.[1,4,13]. Many counter electrode materials have been reported as platinum, carbon-based materials, conducting polymers, metal chalcogenides or oxides, and metal/carbon composites.[5]

1.2.2 Working principle

The generation of photocurrent can be described by the following mechanisms:

1. Absorption

Initially, the photosensitizer absorbs a photon, and the dye molecules excite an electron from the highest occupied molecular orbital (HOMO) in the ground state S to the lowest unoccupied molecular orbital (LUMO) in the excited state S^* through the following reaction.[14]

$$S_{adsorbed} + h\nu \rightarrow S^*_{adsorbed} \, . \tag{1.1}$$
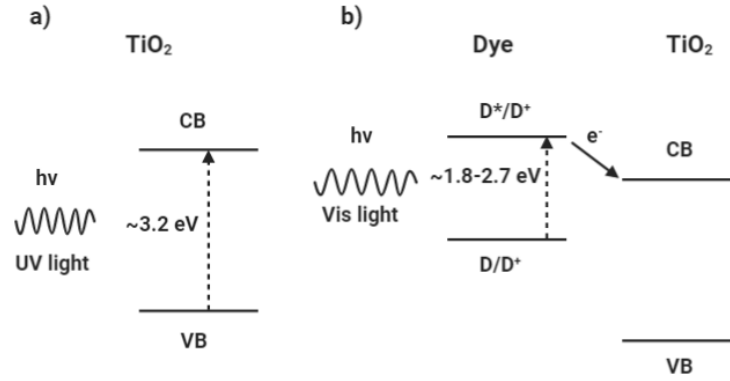
Figure 1.2: Comparison of bands transition mechanism with TiO_2 particles under a) UV irradiation and b) by dye photosensitized particles under visible light irradiation.

2. Injection process

The photoexcited dye injects an excited electron into the conduction band (CB) of the semiconductor (as TiO_2), and the dye molecules that lost an electron are oxidized.[14] The absorption and injection processes are shown in part b of Figure 1.2.

$$S^*_{adsorbed} \rightarrow S^+_{adsorbed} + e^-_{injected} \ . \tag{1.2}$$

3. Energy generation

The injected electrons travel through the network of mesoporous semiconductor film to the conductive substrate. Then, electrons move through the external circuit (or load), where the work performed is delivered as electrical energy, and finally, electrons reach the counter electrode (CE).[8] It is important to mention that the electron transport in the semiconductor film is mainly derived by diffusion due to the electron concentration. This means that at higher light intensities, faster electron diffusion can be obtained.[14]

$$e^-_{injected} + CE \rightarrow e^-_{CE} + electrical \ energy \ . \tag{1.3}$$
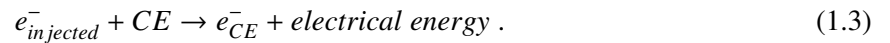
4. Regeneration of dye

The oxidized dye receives an electron from the electrolyte redox couple to replace the lost electron and shifts the oxidized state (S^+) to the ground state (S). If the electrolyte contains the I^-/I_3^- redox couple we have that:[8,14]

$$S^+_{adsorbed} + \frac{3}{2}I^- \rightarrow S_{adsorbed} + \frac{1}{2}I_3^- \; . \tag{1.4}$$
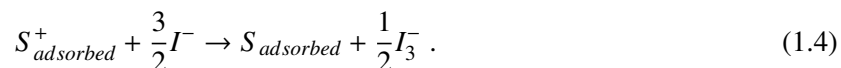
5. Reduction of redox mediator

The electron from the counter electrode is transferred to the electrolyte, and the I^- is regenerated by the reduction of I_3^-, and the regenerative cycle is completed.[3]

$$\frac{1}{2}I_3^- + 2e^-_{CE} \rightarrow \frac{3}{2}I^-_{CE} \; . \tag{1.5}$$

In addition to these mechanisms necessary for the operation of a DSSC, undesirable side processes are simultaneously taking place. These processes correspond to the recombination of injected electrons in the TiO_2 with the oxidized dye or with acceptors in the electrolyte and non-radiative relaxation of the photoexcited dye, which is reflected by the excited state lifetime.[15] Then, processes 2 and 3 must be kinetically more favorable than recombination of injected electrons with the oxidized dye and the electrolyte at the TiO_2 surface for high photocurrent and photovoltage to be generated.[8]

1.2.3 Natural dyes

Natural dyes molecules have been proposed as photosensitizers for DSSCs to provide an alternative way to overcome limitations in the sustainability of using metal complexes and metal-free dyes. Despite the fact that natural dyes have presented a limited performance until now, they have a number of beneficial features such as environmental friendliness, high reduction in the use of noble metals, low production cost, high absorption coefficients, complete biodegradability, easy access, among others.[5] The efficiency of a DSSC is strongly dependent on the type of dye used as sensitizer. Then, it is important to consider that a good photosensitizer should have a high adsorption coefficient, broad visible spectrum to capture sunlight at all wavelengths, higher LUMO energy than the conduction band of semiconductor energy level, strong anchoring groups for adhesion to the semiconductor surface, and rapid regeneration of dye. In the case of natural dyes, the binding energy with the photoanode film, low charge-transfer absorption in the visible spectrum, and stability should be enhanced in order to improve the performance of a DSSC.[14]

Plant pigments occur due to the electronic structure of their molecules, which interacts with sunlight and alter the wavelengths that are either transmitted or reflected by the plant tissue.[16] These pigments can
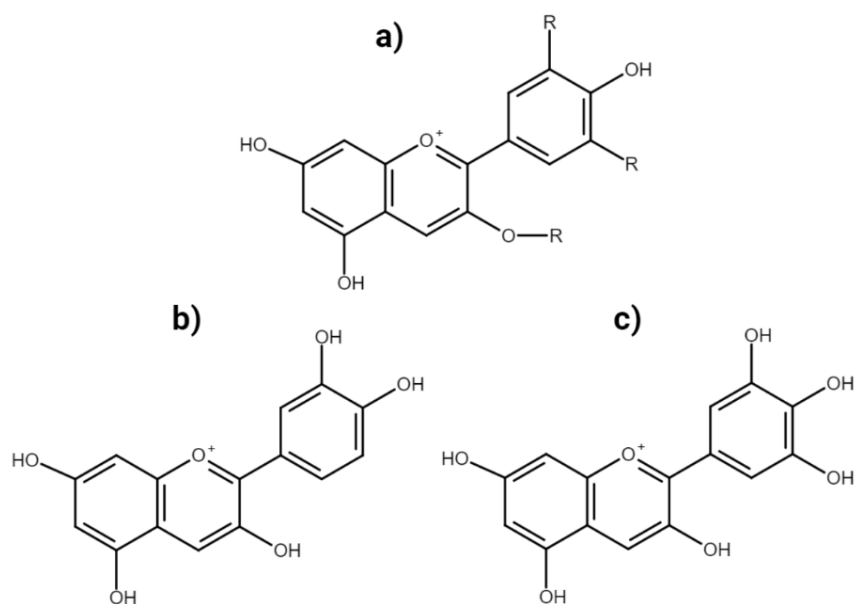
Figure 1.3: Chemical structure of a) anthocyanin and most abundant anthocyanin derivatives b) delphinidin and c) cyanidin in mortiño (Vaccinium floribundum Kunth) and Jamaica flower (Hibiscus sabdariffa L.). Adapted from[3,6]

be extracted from naturally existing colorful pigments in flowers, leaves, fruits, seeds, and various parts of plants. Simple extraction processes based on solvents like water and simple alcohols, as ethanol or methanol, can be used as they are environmentally preferable. Plant pigments can be grouped into four main families: flavonoids (includes anthocyanins), betalains, carotenoids, and chlorophylls.[5]

In this study, the pigments responsible for the absorption of visible light are anthocyanins, which are extracted from mortiño (Vaccinium floribundum Kunth) and Jamaica flower (Hibiscus sabdariffa L.). Anthocyanins constitute a major flavonoid group responsible for different colors ranging from pink to red and violet to dark blue of some flowers, fruits, and leaves of angiosperms.[17] The basic chemical structure of anthocyanins is shown in Figure 1.3 a), which contains carbonyl (-COOH) and hydroxyl (-OH) functional groups that binds to the semiconductor at the photoanode (TiO_2). This attachment stimulates the electron transfer from the anthocyanin molecules to the conduction band of TiO_2.[14] There are 17 different structures reported for anthocyanins[18] and the main ones present in mortiño, and Jamaica flower can be seen in Figure 1.3 corresponding to b) delphinidin and c) cyanidin.[19]

Depending on the sources from where anthocyanins are extracted, their sensitizing performance differs.

Jamaica flower extract used as natural dye sensitizer for DSSCs has been studied in the investigations of Ramírez-Perez et al.[20] and Suhaimi et al.[21] and presented the highest photovoltaic performance among other 11 vegetable dyes used in DSSCs as Mulberry, Cherry Barbados, Oxalis Triangularis, Bawang Sabrang, Harum Manis, Ardisia, Ataco, Achiote, Berenjena, Rábano, Tomate de árbol. On the other hand, mortiño dye sensitizer presented a similar photovoltaic performance in the work of Ramírez-Perez et al. However, research regarding the properties and performance of mortiño extractions used as dye sensitizer in DSSCs is still lacking. To the best of our knowledge, the work of Ramírez-Perez et al.[20] is the only one using mortiño fruit as photosensitizers of DSSCs. The high photovoltaic performance of Jamaica flower and mortiño compared to other vegetable dyes could correspond to a higher concentration of anthocyanins. In this context, Jamaica flowers and mortiño dyes originally and widely available from the Andean sierra of Ecuador are considered as an alternative of anthocyanin source for DSSC preparation.

1.2.4 Photovoltaic performance of a DSSC

The performance of DSSC can be characterized by photovoltaic parameters as open-circuit voltage (V_{oc}), short circuit current density (J_{sc}), fill factor (FF), energy conversion efficiency (η or ECE), maximum power output (P_{max}) and incident photon to current conversion efficiency (IPCE). These parameters are obtained and calculated using photocurrent-voltage (I-V) curves.[8]

The open-circuit voltage (V_{oc}) appears as a bias voltage to annihilate the current generated during illumination when the circuit is open in a solar cell. The V_{oc} corresponds to the electrical potential difference between the energy level of the conduction band of the photoanode at the Fermi level (E_f) and the redox potential of the electrolyte.[17] On the other hand, short circuit current density (J_{sc}) appears at applied zero bias in a solar cell or under a short-circuit irradiation. This value depends strongly on the dye sensitizer's absorption capabilities over a wide spectrum region, the efficient reduction of the oxidized dye by the electrolyte, and the charge carrier mobility at the interaction between TiO_2 and the dye sensitizer. Then, J_{sc} is dependent on incident light and generation of excitons.[6]

Another important parameter in the performance of a solar cell is the fill factor (FF), which is a measure of the junction quality and series resistance of the DSSC. The maximum FF value can be one, but in a DSSC, it is lower due to resistances present in the cell. Then, electron transport resistance through the TiO_2 matrix, ion transport resistance, charge transfer resistance at the counter electrode, and sheet resistance of the substrate and counter electrode are present.[6] FF can be represented by Eq. 1.6:

$$FF\% = \frac{P_{max}}{J_{sc}V_{oc}} = \frac{J_{max}V_{max}}{J_{sc}V_{oc}} , \tag{1.6}$$

where J_{max} and V_{max} are the maximum current density and the maximum voltage, respectively.

The power conversion efficiency (η) is a measure of the output power of the DSSC and the conversion of light into electricity. The ECE is defined as the ratio of the maximum output electrical power (P_{max}) and the incident light power (P_{in}).[17]

$$\eta = \frac{P_{max}}{P_{in}} = \frac{J_{sc}V_{oc}FF}{P_{in}} \ .$$

(1.7)

Also, the external quantum efficiency (EQE) or incident-photon-to-electron conversion efficiency (IPCE) is used to obtain the photocurrent action spectrum for dye evaluation.[6] The IPCE is defined as the ratio between the number of electrons flowing through the external circuit to the number of photons incident on the cell surface at any wavelength λ.[16] It is given by the following expression:

$$IPCE\%(\lambda) = \frac{n_{electrons}}{n_{photons}} = 1240(eVnm)\frac{J_{sc}(mAcm^{-2})}{P_{in}(mWcm^{-2})\lambda(nm)} \ .$$

(1.8)

Usually, these photovoltaic parameters are assessed under test conditions based on Suns's emission spectrum with a radiant intensity of 100 mW/cm^2 and model atmosphere "Air Mass 1.5 Global" (AM1.5G) spectrum.[17]

1.3   Standardised Solar Spectrum and Solar Irradiation

The sun's radiation at the Earth's surface depends on factors such as atmospheric effects, atmospheric variations, latitude differences, and time of day. As solar cells' different parameters and efficiency are sensitive to variations in the power and spectrum of radiation of the incident light, a standard spectrum and power density have been standardized outside the Earth's atmosphere and at the Earth's surface. This allows an accurate comparison and evaluation between PV devices at different times and locations.[22]

The standard global AM 1.5G solar irradiation at Earth's surface spectrum is formed using specific atmospheric conditions as absolute air mass of 1.5 (solar zenith angle $48.19^{o}s$), total column water vapor equivalent of 1.42 cm, total column ozone equivalent of 0.34 cm, among others. In this case, the surface receiving the solar radiation is an inclined plane at 37° tilt from the horizontal.[22] AM 1.5G standard comprises the global direct and diffuse radiation, which power density has been normalized to 100 $mWcm^{-1}$. Both radiation spectrums are present in the ASTM G-173-03 reference spectra. The air mass (AM) refers to the path length of the direct solar radiation through the atmosphere and is a measure of the reduction in the power of light as it passes through the atmosphere.[23] On the other hand, the air mass zero (AM0) corresponds to the standard spectrum outside the Earth's atmosphere.[22]

1.4 Carbon Nanotubes

Carbon structures corresponds to different crystalline modifications called carbon allotropes. They result from the flexible electron configuration of carbon atoms, which has six electrons and the 2s orbital and one, two or three of the 2p orbitals can form an sp, sp^2 or sp^3 hybrid, respectively.[24] Carbon nanotubes are quasi-one dimensional crystals made of one or more concentric shells of graphene sheets.[25] Depending on the number of rolled up sheets, CNTs can be classified into single-wall or multi-walled nanotubes with typical diameters of SWCNTs and MWCNTs of 0.8-2 nm and 5-20 nm, respectively.[1] The chemical bonding of nanotubes is composed entirely of sp^2 hybridized bonds, similar to those of graphene. Each carbon atom is connected to the other three atoms, while a free-electron delocalized in the p_z orbital moves along an electron cloud.[26]

Carbon nanotubes exhibit remarkable mechanical[27], electrical[25], and thermal properties properties[28]. For this reason, many possible applications in nanodevice engineering and technological applications are in constant research. It is important to mention that the physical properties, as the metallic or semiconductor character of SWCNTs, can vary significantly depending sensitively on the microscopic structure of the tube.[24] SWCNTs are usually labeled in terms of the graphene lattice vectors a_1 and a_2, where the graphene sheet is rolled up in such a way that a graphene lattice vector $c = na_1 + ma_2$ becomes the circumference of the tube as can be seen in Figure 1.4. This vector is known as chiral vector and controls the diameter, chiral angle of the nanotube, the unit cell's length, and the number of carbon atoms in the unit cell. The diameter of a tube is directly related to the chiral vector c by:[25]

$$d = \frac{|c|}{\pi} = \frac{a_o}{\pi} \sqrt{n^2 + nm + m^2} \, , \tag{1.9}$$

the pair of integer indexes (n, m) are called the chiral index of a tube. The other parameter, which is the chiral angle θ specifies the arrangement of the graphene hexagons on the wall of the tube. This parameter is related to the chiral index by:[25]

$$cos(\theta) = \frac{c \cdot a_1}{|c| \cdot |a_1|} = \frac{an + m}{2 \sqrt{n^2 + nm + m^2}} \, , \tag{1.10}$$

the allowed values for the chiral angle vary between $0^o \leq \theta \leq 30^o$ and depending on it, SWCNTs are classified on three chiralities: armchair, zigzag and chiral. In the case of a chiral angle of 0° or 30°, the tube has a particular high symmetry corresponding to zigzgag ($\theta = 0^o$) (n,0) and armchair ($\theta = 30^o$) (n,n) tubes. They are called achiral nanotubes. All other existing SWCNTs are chiral ones with ($n = arbitrary, m \neq n \neq 0$) chiral index.[25] The electronic properties of a SWCNT depends on its structural indices (n,m).[29]

a)   b)
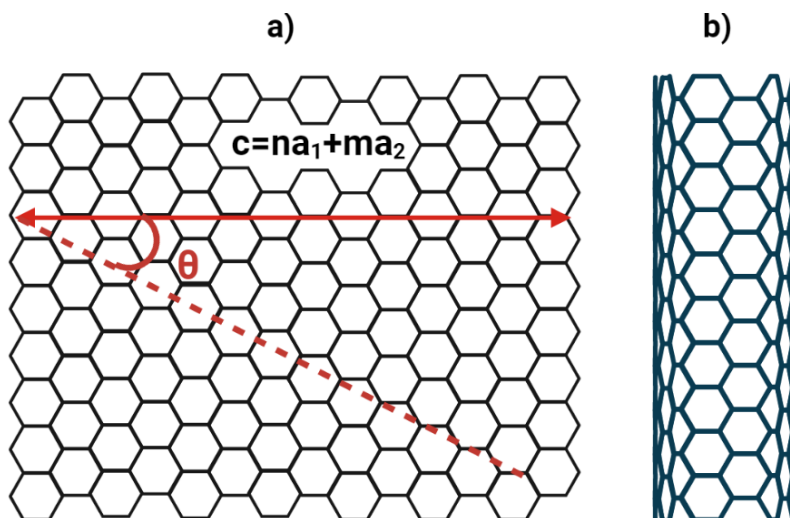
Figure 1.4: Scheme of a carbon nanotube strucutre. In a) graphene sheet, where a chiral vector c can be specified by a chiral index (n,m) using basis vectors a_1 and a_2 from graphene. When rolled up it forms b) a seamless cylinder.[25]

The main synthesis methods to produce carbon nanotubes that have been developed over the past years are laser ablation, arc-discharge, and chemical vapor deposition. These growth processes present a carbon plasma that is formed either by heating or by chemical decomposition. The use of a catalyst added to this plasma is necessary in most cases for the growth of the tubes.[25]

1.4.1   Carbon nanotubes at DSSC counter electrode

In a DSSC counter electrode, the transparent conductive oxide (TCO) glass as fluorine-doped tin oxide (FTO) and indium tin oxide (ITO) present an extremely low reduction reaction of the electrolyte (in this case I_3^-/I^-). For minimizing the charge transfer overpotential, catalytic materials are coated on TCO glass at the counter electrode to speed up the reaction.[1] Platinum has been the most used counter electrode material for DSSCs, but it presents a high cost and degrades over time in the electrolyte of DSSCs. In order to replace the conventional Pt and other expensive metal metals, CNTs are promising candidates as counter electrode materials. This is because, they can present high catalytic activity, high conductivity, high surface area, and high corrosion chemical resistance.[10,30]

Both SWCNTs and MWCNTs were reported as the counter electrode of DSSCs. Mei et al.[30] used SWCNTs or MWCNTs as counter electrodes by dispersing them in polyethylene glycol (PEG), coating the

gel on FTO glass, and removing the PEG from the CNT films through heating. The DSSCs formed with both electrodes exhibited a power conversion efficiency (PCE) comparable with that of the conventional Pt counter electrode. In another study, Nam et al.[31] prepared randomly dispersed MWCNT paste and screen-printed it on FTO glass as counter electrode obtaining a PCE of 8.03 %. Also, they prepared relatively well-aligned CNTs by directly growing the CNTs from catalytic chemical vapor deposition obtaining a PCE of 10.04 %, which is higher from the Pt-coated counter electrode (PCE=8.80 %). In this study, SWCNTs are used as counter electrode catalyst deposited on FTO glass. The main reason behind using SWCNTs instead of MWCNTs is because of better stability in photovoltaic performance.[31]

1.4.2   Carbon nanotubes gels

Different methods to improve the process capabilities of CNTs in solvents have been developed up to now.[32] Among them, Fukushima et al.[33,34] reported a method to form gels of CNTs and ionic liquids, which formation is related to the normal van der Waals interaction between CNTs and ionic surfactants. Some applications of CNTs gels using this method are present in actuators, electrochemistry, biology, and dispersion of CNTs in water. Later, Mei & Ouyang[32] demonstrated that CNTs could form gels with some liquid organic compounds. Incorporating dispersed CNTs into a polymer matrix allows the fabrication of gels, which corresponds to a dispersion of molecules of a liquid within a solid medium. An important application of these gels is the fabrication of conductive CNT films by coating the CNT gels on a substrate and removing the organic compounds through heating.[32] Mei et al.[30] fabricated binder-free SWCNT films using PEG as organic solvent by mechanical grinding for their use in DSSCs as explained in the last section.

1.5   Titanium dioxide

Titanium dioxide is a wide bandgap semiconductor (2.8-3.3 eV) material that has been applied in areas as photocatalysis, photovoltaics, water, and air purification, energy conversion, and sensing.[35] This is mainly because TiO_2 nanostructures present several advantages as the presence in different phases, morphology, low-cost, non-toxicity, high abundance in nature, and slower charge carrier recombination process.[36]

In general, TiO_2 exists in three crystalline phases: anatase, rutile, and brookite. Anatase and rutile crystalline phases present a tetragonal structure, and brookite presents an orthorhombic structure.[36] The three forms differ in their bandgap, having 3.05, 3.20 eV, and 3.28 eV for rutile, anatase, and brookite, respectively. For photovoltaics applications, as efficient photoanode material anatase phase presents high surface area, high coefficient of electron diffusion, and low dielectric constant, for which is considered

an ideal candidate compared to rutile. On the other hand, brookite is not recommended because of its complex synthesis process.[10]

As the photoelectric conversion relies on the energy bandgap of the semiconductor, TiO_2 possesses only the desired performance in utilizing ultraviolet light for photovoltaics. Then, its overall solar activity is limited and visible light can not be used in principle. To extend the response of TiO_2 to longer wavelengths, surface modification strategies such as dye sensitization are used.[37] For DSSCs, the optical properties and electronic transport properties of TiO_2 films on transparent conductive oxide (TCO) depend on the fabrication process and the phase of the material. Methods of production of TiO_2 nanoparticles include sol-gel method, chemical vapor deposition (CVD), magnetron sputtering, hydrothermal method, flame spray pyrolysis (FSP).[38–40]

1.6   Characterization techniques

1.6.1   UV-Visible Spectroscopy (UV-Vis)

UV-Vis spectroscopy is one of the most used techniques for measuring absorbing species of a wide range of compounds. Besides, this technique can provide detailed information about the properties of molecules.[41] The UV region of the electromagnetic spectrum is found in the range of 200 to 350 nm and the visible region in the 350 to 700 nm. As one process resulting from the interaction between electromagnetic radiation and matter is absorption, its working principle in this UV-Vis region is linked to the electronic transition in molecules. When a photon from electromagnetic radiation is absorbed, electronic transition occurs from bonding (σ and π) and/or non-bonding orbitals to antibonding orbitals (σ^* and π^*).[42]

The measurements in UV-Vis spectroscopy are based on a beam of light of intensity I_o incident on some absorbing sample, and the amount of light absorbed by an analyte in a homogeneous isotropic medium is proportional to the amount of analyte in the sample. This is known as the Beer-Lambert law, which states that:[42]

$$A = log(\frac{I_o}{I}) = \varepsilon(\nu)lC \ , \tag{1.11}$$

where A is the absorbance, ε is absorptivity, l is path length through the solution, and C is the concentration of the species absorbing light. The instrumentation of a UV-Vis spectrophotometer light from a source is passed from a slit or collimator to a monochromator to isolate a specific group of wavelengths. Then, it is passed through an exit slit to the sample where a specific wavelength is absorbed, and finally, the light reaches the detector.[42] The main components of a simple spectrophotometer are present in Figure 1.5.

UV-Vis spectroscopy is used in this study to determine the range of optical absorption of the natural
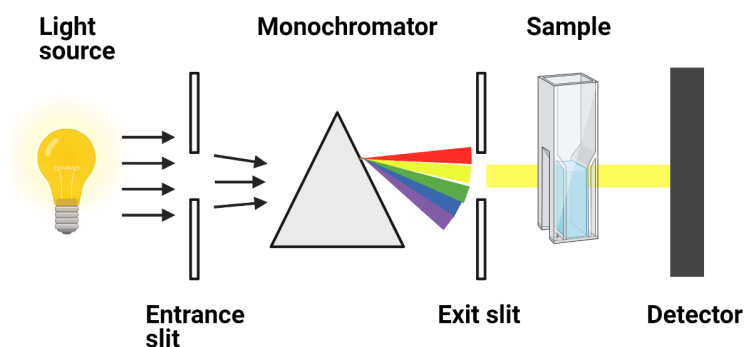
Figure 1.5: Schematic diagram of a simple UV-Vis spectrometer instrumentation formed by a light source, slits, monochromator and detector. The monochromator and slits arrangement is used to isolate a specific group of wavelengths that reaches the sample.
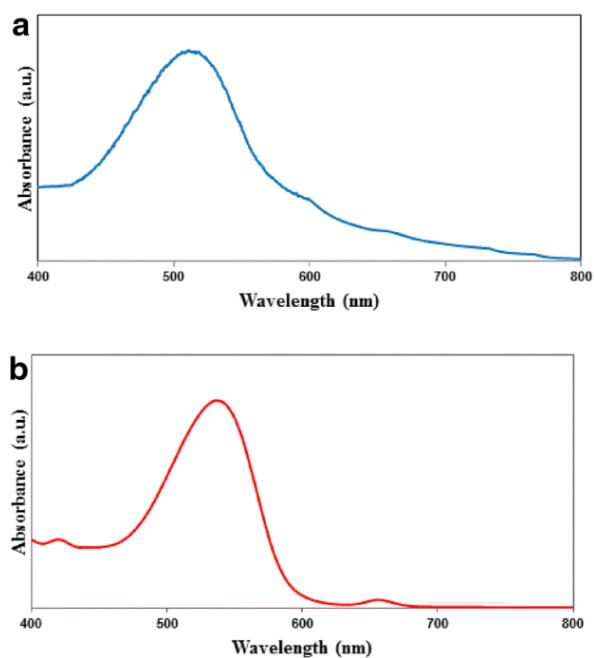
Figure 1.6: Absorption spectrum of a) Jamaica flower and b) mortiño ethanol extract solutions at pH 1 from Ramírez-Perez et al.[20] work.

dyes extracted from mortiño (accinium floribundum Kunth) and Jamaica flower (Hibiscus sabdariffaL.). Sensitizers for DSSCs need to present a high absorption response in the visible and near-infrared regions of

the solar spectrum and the absorption spectrum of a dye is a key factor to study to enhance the performance of DSSCs. The compound present in mortiño and Jamaica flower that acts as a photosensitizer is anthocyanin. Generally, anthocyanins show a broad absorption band in the visible region due to charge transfer transitions from HOMO to LUMO[43] in the range of 450–600 nm of the spectrum.[16] In this work, it is expected to obtain broadband absorption in this range from the mortiño and Jamaica extracts. In addition, the influence of pH in the dye extraction process can be studied by comparing the results of Ramírez-Perez et al.[20] (Figure 1.6) using ethanol extract solutions at pH of 1 with this study using a neutral pH.

1.6.2 Current-Voltage (IV) curve
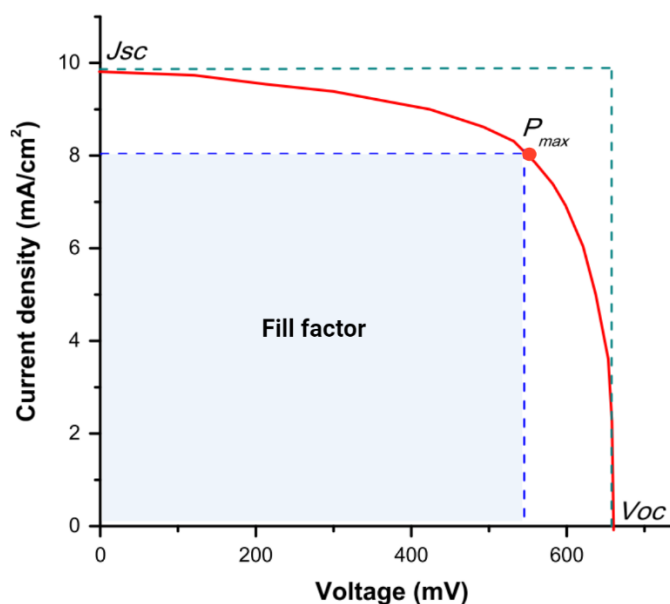
Figure 1.7: Characteristic current density vs volatge (J-V) curve from a solar cell, where values of J_{sc}, V_{oc}, P_{max} and fill factor can be extracted to evaluate the cells performance. Adapted from Kumara N. et al.[8]

The I-V curve is one of various graphical methods to characterize an electronic device. The graphic obtained establish the type of behavior, like a resistance, diode, current source, voltage source, etc. A solar or PV cell output voltage and current are dependent on each other and determined by the power converter connected to their terminals.[44] Then, the I-V curve of a solar or PV cell is the most important and widely used to characterize its electrical behavior and energy generation capacity under certain conditions

of temperature and irradiance.[45] The I–V curve of a solar cell is described by a set of parameters, such as the open-circuit voltage (V_{oc}), short circuit current density (J_{sc}), and maximum power output (P_{max}). These parameters are presented in Section 1.2.4 and can be seen in Figure 1.7 from a current density vs. voltage curve. Also, the P-V characteristic curve (power as a function of voltage) can be obtained in order to determine the maximum power supplied by the source under specific conditions.[44]
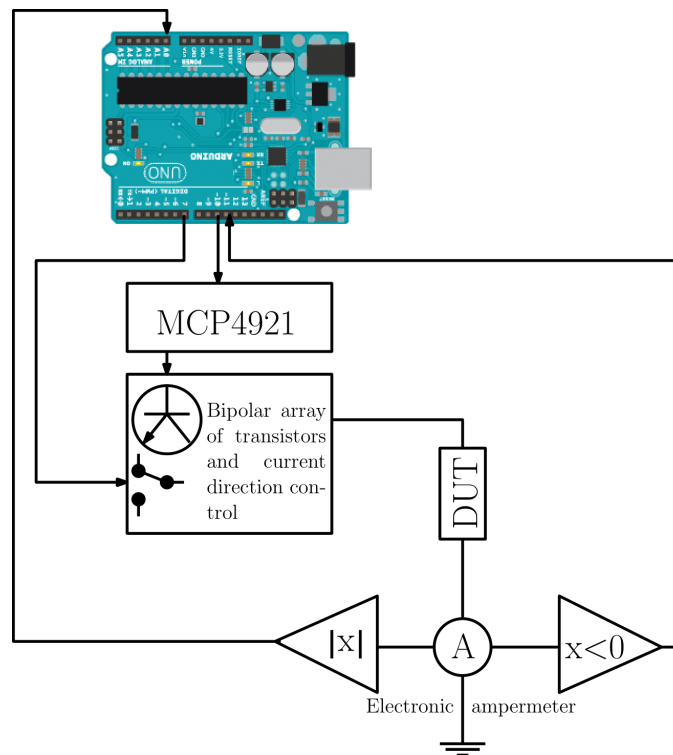
Figure 1.8: Schematic diagram of the equipment used to measure the I-V curves of the fabricated DSSCs.

The working principle of an I-V curve measure is based on the control of the current supplied by the solar cell between V_{oc} and J_{sc} values, where each operating point is defined by a current and voltage value. There are various methods two obtain IV curves: Variable resistor, Capacitive load, Electronic load, Bipolar Power Amplifier, Four-quadrant power supply, DC-DC Converter.[46] In order to monitor the operating conditions, external components as temperature and irradiance sensors can be used.[44] For this work a Bipolar Power Amplifier system was used to obtain the IV curves. Figure 1.8 show the schematic block of the equipment used to measure the IV curves of the different built cells. An Arduino is the kernel of the control and communications with the computer, a bipolar circuit is used as the load for the devise

under test (DUT). Since arduino and MPC4921 only can work with positive voltage an extra circuitry was dispose for reversal the current direction and to read negative currents.

1.6.3   Raman spectroscopy

Raman is a spectroscopic technique based on inelastic light scattering, and it is used to determine the vibrational, rotational, and other modes of a system.[47] When light interacts with matter, the photons may be absorbed, scattered, or may not interact with the material. In the case of a scattering process, the light interacts with the molecule and polarizes the cloud of electrons around the nuclei to form a short-lived state called a "virtual state" from which photons are quickly re-radiated. Predominantly, light is elastically scattered (Rayleigh scattering), which means that the energy of the scattered photon is equal to that of the incident photon[48], as can be seen in Figure 1.9 (a). On the other hand, in a Raman or inelastic light scattering process, an incident photon with energy $E_i = E_{laser}$ and momentum $k_i = k_{laser}$ scattered at the sample results in a photon with different energy E_s and momentum K_s. By energy and momentum conservation:[49]

$$E_s = E_i \pm E_q \ \ and \ \ k_s = k_i \pm q \, , \tag{1.12}$$

where E_q and q are the energy and momentum change of the photon during the scattering event. When a molecule from the ground state absorbs energy from the laser beam, its promoted to a higher excited vibrational state, and the emitted radiation is of lower energy than the incident radiation. This process corresponds to a Stokes scattering represented in Figure 1.9 (b). However, some molecules can be present initially in an excited vibrational level due to thermal energy, and the emitted radiation is of higher energy than the incident radiation, known as anti-Stokes scattered[48] and represented in Figure 1.9 (c).

When a sample is illuminated with a laser light source, a Raman spectra can be observed by passing the scattered light (collected by the lens) through a monochromator that divides the light entering the instrument into the scattered light on the lower energy side relative to the incident light (Stokes scattering) and the scattered light on the higher energy side (anti-Stokes scattering). When there is no shift in energy corresponding to the frequency of the laser line, a strong Rayleigh signal is present, which can be eliminated by using a so-called notch filter or a (triple) monochromator. The final Raman intensity of each spectral line is measured by counting the number of photons recorded for that line and by considering the instrument function of the monochromator and the CCD detector to get a properly calibrated Raman signal. It is essential to mention that the shifts in energy give information about the vibrational modes (phonons) of the molecules in the system, and when the laser energy E_{laser} or scattered light energy matches an
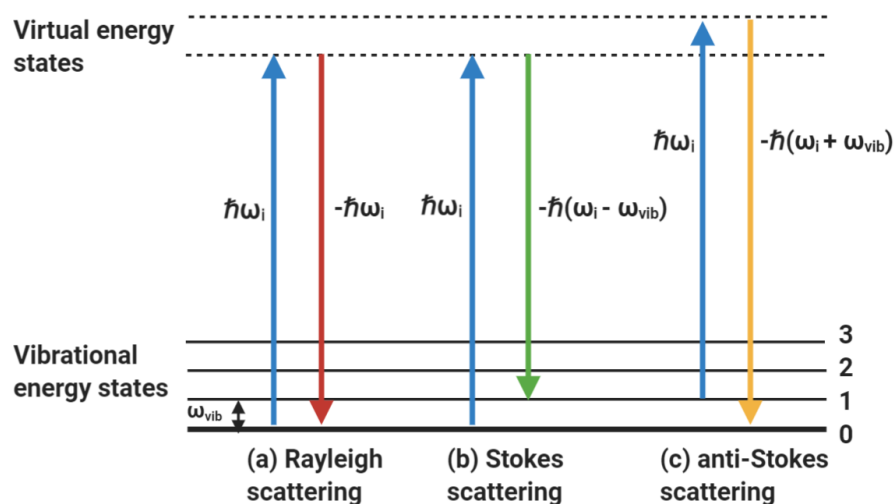
Figure 1.9: Scheme of light scattering processes: (a) Rayleigh scattering, (b) Stokes scattering and (c) anti-Stokes scattering. The arrows represent the incident and scattered photon energies and the vibrational excitation frequency is represented by ω_{vib}.

optical transition E_{ii} in the scattering system, resonance effects occur, and the Raman signal is strongly enhanced.[49]

Raman spectroscopy has provided an important tool regarding the analysis and characterization of carbon-based materials, this technique provides information about chemical structure, the introduction of impurities, defects, electron-phonon interaction, nanotube diameter, among others.[49,50] For SWCNTs, many features can be identified in a Raman spectrum such as the radial breathing mode (RBM), the G-band, the dispersive disorder induced D-band, and it's second-order related harmonic $G' - band$. RBMs corresponds to the normal mode vibration where the carbon atoms vibrate in phase in the radial direction.[51] In particular, RBM modes are typically found between $\sim 100cm^{-1}$ to $400cm^{-1}$ and the frequency of an RBM peak (ω_{RBM}) depends on the tube diameter following the following relation:[25]

$$\omega_{RBM} = \frac{A}{d} + B \,, \tag{1.13}$$

where A and B are constant coefficients and vary widely in the literature. These values depend on several factors as growth methods, dispersion environment, the substrate, among other environmental conditions.[49] In order to determine the chiralities of a SWCNTs sample, it is necessary to obtain a Kataura plot, where resonance energies (E_{ii}) for each (n, m) SWNTs as a function of the SWNT diameter are plotted.

The transition or resonance energies (E_{ii}) can be obtained by using various laser excitation frequencies (E_{laser}).[49]
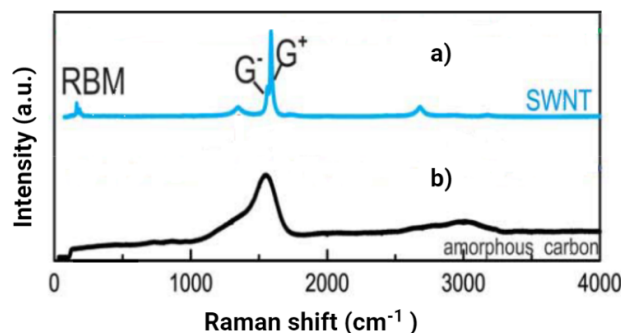
Figure 1.10: Raman spectra of (a) SWCNTs bundle sample and (b) amorphous carbon. Adapted from Dresselhaus M. et al.[50].

The origin of the G peak corresponds to tangential modes from the optical phonons of graphite. The tangential modes involve an out-of-phase displacement of two neighboring carbon atoms, especially sp^2 in-plane carbon-carbon bonds. In the case of SWCNTs, it corresponds to a multicomponent high energy frequency (around 1500-1600 cm^{-1}) feature[51], where two, four, or six G-band phonons are allowed in this first-order G-band. Two of these modes dominate the spectra, corresponding to G^+ and G^- peaks. The G^- feature depends strongly on the electronic nature of the tubes (metallic and semiconducting) as well as on changes on the Fermi level.[29]

D-band corresponds to tangential modes related to the presence of disorder or defects that activates certain vibrational modes. It is related to the break of the crystal symmetry of graphene, 3D graphite, and carbon nanotubes due to the introduction of defects. This feature is highly dispersive as a function of the laser energy used.[49] Another important feature is the G'-band, which comes from a second-order symmetry-allowed Raman process involving two scattering events. In the case of the G'-band, there is a two-phonon Raman process. Figure 1.10 (a) shows the spectra of an SWCNTs bundle sample, which exhibits the characteristic RBM, D, G^-, G^+ and G' bands coming from the vibrational modes of SWCNTs. Also, amorphous carbon Raman spectra is presented in 1.10 (b) where a wide feature can be seen corresponding to D and G peaks.[49]

Raman spectroscopy is used in this study for the characterization of SWCNTs dispersion, SWCNTs film deposition on the counter electrode, and identify if the crystalline structure of the SWCNTs and their distribution remains after the film deposition process. The followed methodology for the SWCNTs

film deposition at the counter electrode involves the addition of PEG and heating treatment. After this deposition structural changes (defects) in the SWCNTs structure and the presence of PEG could hinder the performance of the DSSCs. Also, Raman spectroscopy is used to characterize the candle soot film on the counter electrode. According to Zhang et al.[52] candle soot is constituted of carbon particles with the presence of amorphous carbon, which Raman spectra can be seen in Figure 1.10 part b).

1.6.4 X-ray diffraction (XRD)

X-ray diffraction is a non-destructive analytical technique for the study of crystalline structures. The working principle of X-ray diffraction is based on constructive interference produced with the interaction of monochromatic X-rays that are scattered at specific angles from a different set of lattice planes present in the material. This constructive interference is present when conditions satisfy Bragg´s law ($n\lambda = 2d\sin\theta$). Where n is a positive integer, λ is the wavelength of the X-rays, d is the interplanar distance generating the diffraction, and θ is the diffraction angle. Scanning the sample in 2θ range angles should cause that all possible diffraction directions of the lattice to be measured due to the random orientation of the powdered material. From the diffraction peaks, the atomic positions within the lattice planes and interplanar distance allow the identification of compounds or periodic atomic arrangements in a given material.[53] Also, this identification needs the comparison of d-spacings with standards reference patterns in a database. X-ray diffraction provides detailed information about the crystallographic structure, chemical composition, and other structural parameters of a material, such as average grain size, crystallinity, and strain.[54]

An X-ray diffractometer is formed by three basic elements: an X-ray tube, a sample holder, and an X-ray detector. The X-rays are produced in a cathode ray tube, where the most common target material for single-crystal diffraction is copper, obtaining Cu K_α X-rays (λ=0.15406 nm). Then, the X-rays are filtered to produce monochromatic radiation, collimated, and directed to the sample. As the sample and detector are rotated 2θ angles, Bragg peaks are recorded in a detector.[53] In order to relate the diffraction peaks with the crystallite size of a sample, the Scherrer equation is used:[55]

$$D = \frac{K\lambda}{\beta cos\theta} ,$$

(1.14)

where D is the crystallite size, K is the shape factor (0.89), λ is the wavelength of radiation ($Cu_{K\alpha}$ λ=0.15405 nm), θ is the diffracted angle of the peak, and β is the full width at half maximum of the peak. In addition, broadening in the peaks is related to physical broadening and instrumental broadening. Then, for decreasing the instrumental error, a correction responsible for crystal size should be added by substracting the squares of the measured broadening with the instrumental broadening.[55]
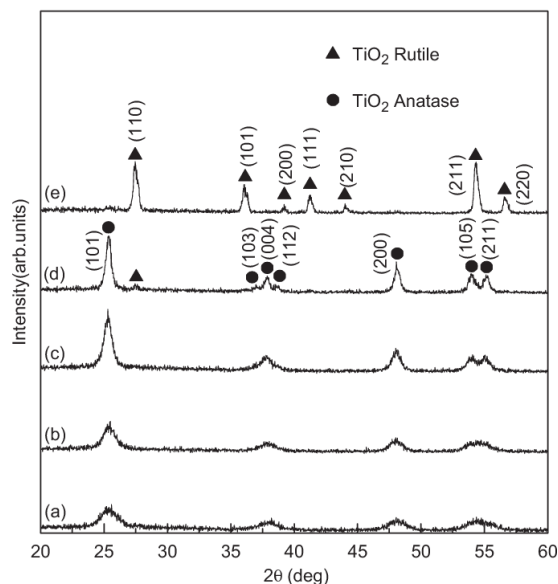
Figure 1.11: X-ray diffraction patterns of TiO2 films sintered at different temperatures (a) as deposited, (b) sintered at 400 ^oC, (c) sintered at 500 ^oC, (d) sintered at 600 ^oC and (e) sintered at 700 ^oC from the work of Meen et al.[56]

In this case, X-ray diffraction is used for the identification of titanium dioxide anatase and rutile crystalline phases in commercial and treated (sintered film) samples. The study of the presence of TiO_2 anatase phase at the photoanode of a DSSC is necessary as the anatase phase presents a higher surface area, higher coefficient of electron diffusion, and a low dielectric constant compared to the rutile phase.[10] Figure 1.10 shows the XRD patterns of TiO2 films sintered at different temperatures. Literal c) corresponds to TiO2 film sintered at 500 ^oC, which are considered as the best anatase phase by the work of Meen et al.[56] At higher temperatures, it can be seen a phase transition from anatase to rutile, which is not beneficial.

Chapter 2

Motivation

As the worldwide energy demand is increasing with the growth of world population, industrial developments, and the advancement of technology, renewable energy sources (RES) are expected to significantly play an important contribution to the sustainable energy supply. The International Energy Agency (IEA, 2019) states that the contribution of the RES provides two-thirds of the total power generation by 2040 globally, with solar photovoltaics (PV) being the largest source of energy surpassing the others by 2035.[14,57] Emerging PV and specifically Dye-Sensitized Solar Cells (DSSCs) present an alternative to the well-established PV devices made from silicon due to its exceptional low-cost materials, ease to fabricate and assemble, as well as environmentally friendliness. Also, it can perform even under diffuse light conditions.[58] In this context, DSSCs have attracted a lot of attention and research intending to develop highly efficient DSSCs components achieving efficiencies of ~ 14% and ~ 33% under indoor illumination (i.e., 1000 lux).[5] Given the extensive use of DSSCs, their different components (previously discussed in Section 1.2.1) could be improved by targeting the cost, stability, durability, and performances of each one.

The most widely employed dye sensitizers are inorganic metal dyes, especially ruthenium-based dyes. However, the process of synthesizing these dyes is laborious, costly, and involves the use of toxic materials. In that concern, natural dyes or pigments easily obtained from fruits, flowers, leaves, seeds, barks, and various parts of plants have been extracted and investigated as photosensitizers.[8] Despite the limited efficiency that natural dyes have demonstrated, they present some advantages as high absorption coefficients, low cost, and energy-saving production, easily available and abundant in nature, non-toxic, and complete biodegradability. Among natural pigments, anthocyanins are the most abundant ones of the flavonoid family and exhibit broadband in the VIS region of the spectrum, ascribed to charge transfer transitions.[5] In this project, a simple extraction process based on ethanol as solvent is used to extract

anthocyanins from mortiño (Vaccinium floribundum Kunth) and Jamaica flower (Hibiscus sabdariffa L.), which already have been used as sensitizers in DSSCs.[20]

In the case of the counter electrode fabrication, many CE materials have been reported as platinum, carbon-based materials, conducting polymers, metal chalcogenides or oxides, nitrides, and metal/carbon composites.[5] Among them, carbon nanotubes are promising to substitute the conventional CE made of platinum. Better stability in photovoltaic performance, high electrical conductivity, and good electrocatalytic activity have been reported using SWCNTs as the counter electrode.[1,30,59] The fabrication methodology of the SWCNTs films on fluorine doped tin oxide (FTO) coated conductive glass used in this project is similar to the work of Mei X. et al.[30], in the sense that it involves the presence of a binder (polyethylene glycol) to form a gel, which is subsequently deposited and heated.

This graduation project aims to study the photovoltaic activity and performance of DSSCs using natural dyes extracted from mortiño (Vaccinium floribundum Kunth) and Jamaica flower (Hibiscus sabdariffa L.), as well as the use of SWCNTs as counter electrode material. Moreover, the study focuses on the effect of the sensitization time at which the photoanode is soaked in the natural dyes. As the properties of each component in a DSSC play a key role in the final photovoltaic performance, the compositional and structural properties of the photoanode and counter electrode films with their respective film deposition methodologies are examined. The absorption properties of the extracted natural dyes are also examined.

2.1   Problem Statement

By modulating and studying the physical properties of the different components of a dye-sensitized solar cell, they can be optimized, taking into account the cost-effectiveness. In this context, the use of nanomaterials as SWCNTs at the counter electrode could enhance the electrocatalytic activity and stability in the photovoltaic performance of a DSSC. On the other hand, the use of natural dyes presents many advantages like low cost, easily available, abundant in nature, and non-toxic when compared with other dye sensitizers.

2.2   General and Specific Objectives

2.2.1   General objective

Develop and study the properties of DSSCs using mortiño and Jamaica flower natural dyes as sensitizers with SWCNTs and candle soot films used as counter electrodes.

2.2.2 Specific objectives

- Analyze the effect of sensitization time of the TiO_2 film with the dyes at the photoanode.

- Identify the effect of the film deposition process and the heat treatment on the structure of the SWCNTs film.

- Characterize the crystalline phases of TiO_2 present in raw commercial sample and sintered deposited films at the photoanode.

- Evaluate the absorption range in the visible range of the natural dye extractions using UV-Vis spectroscopy.

- Correlate the results of photovoltaic performance from the different DSSCs structures with the charge generation and transport phenomena acting in the DSSCs.

Chapter 3

Methodology

3.1 Chemicals and materials

Polyethylene Glycol 400 (PEG400), acetic acid (CH_3COOH) 30 wt% and titanium dioxide powder 98% (TiO_2) were purchased from LOBAChemie. Absolute ethanol 99%, metallic iodine (I) and potassium iodide (KI) were purchased at *M&M* representations. All chemicals were used as received without further modification. Fluorine doped tin oxide (FTO) coated glass, sheet resistance 10 Ω/sq, 2.2 mm thick, was used both at the photo-anode and at the counter electrode.

3.2 Extraction of natural dye sensitizers

The natural dyes used in this study were extracted from mortiño and Jamaica flower using absolute ethanol as the extraction solvent. For this purpose, 5 g of mortiño and dry Jamaica flowers were weighted and subsequently crushed in a mortar until obtaining a paste and a fine powder, respectively. Then, each sample was mixed with 50 mL absolute ethanol in a beaker and stirred magnetically for 3 h at 45 ^oC. The beaker was covered using aluminum foil to prevent evaporation of the solvent[60]. The solids were filtered to acquire a pure vegetable dye solution and were stored covered in aluminum foil in a refrigerator. The process can be seen in Figure 3.1.
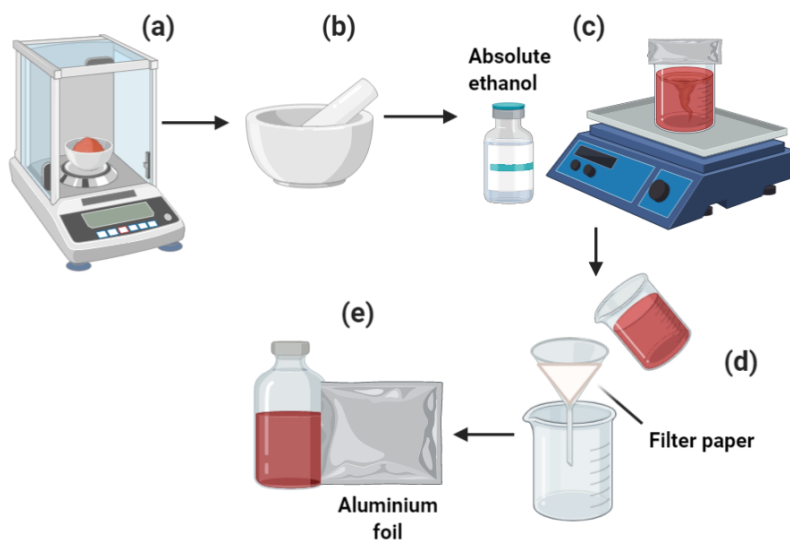
Figure 3.1: Extraction Process of the natural dye sensitizers. It is described by (a) mortiño and Jamaica flower weighing, (b) mortiño and Jamaica flower crushing in a mortar, (c) sample mixing with absolute ethanol and stirring, (d) filtering process of each sample and (e) storing after covering with aluminum foil.

3.3   Preparation of photoelectrodes

In order to prepare the TiO_2 paste for the film deposition onto the AZO glass, 20.57 g of TiO_2 powder was mixed with 15 mL of 10% dilute glacial acetic acid and ground in a mortar. To this, 2.2 mL of polyethylene glycol (PEG) and few drops of Triton X100 were added, and the mixture was ground for 10 minutes to produce a homogeneous adhesive paste. In this case, PEG is used as a binder, Triton X was implemented to facilitate the separation of colloid, and the diluted acetic acid was added to enhance the adhesion to the substrate and prevent the formation of cracks[38,61]. Then, the paste was coated using a glass slide on the FTO conductive glass substrates with Kapton tape at the edges forming rectangles of 1x1.5 cm. The films were allowed to dry in ambient for 10 minutes, and the Kapton tape was removed. Finally, the samples were sintered at 450 ^oC for 30 minutes to achieve the anatase crystal phase of the TiO_2.

3.4   Preparation of counter electrodes

Before deposition of SWCNTs and candle soot films, FTO conductive glass plates were cleaned in a detergent solution and rinsed with abundant distilled water and ethanol.

3.4.1 SWCNTs film deposition

The initial material was an aqueous solution dispersion of 0.04 wt.% SWCNTs with 1 wt.% of SDS. 1mL of the dispersion was mixed with 0.8 mL of acetone and sonicated for one hour. Acetone is used as according to Rossi et al.[62] work, acetone was the most effective organic solvent at interrupting the SDS:SWCNT interaction without producing deleterious side reactions or causing precipitation of the surfactant. Then, the solution was centrifuged in a Gusto HEA10050 centrifuge at 10000 rpm for 45 minutes in order to remove the supernatant and get rid of the excess SDS. The method to obtain gel-coated binder-free SWCNTs films deposited onto the FTO coated conductive glass was performed taking into account the procedure of Mei X. et al.[30] So, 0.4 mL of polyethylene glycol (PEG) was added, agitated in a vortex mixer, and subsequently sonicated for 15 minutes. This process was repeated in two additional Eppendorfs in order to obtain enough amount of a black CNT/PEG gel. A schematic diagram of the process can be seen in Figure 3.2.
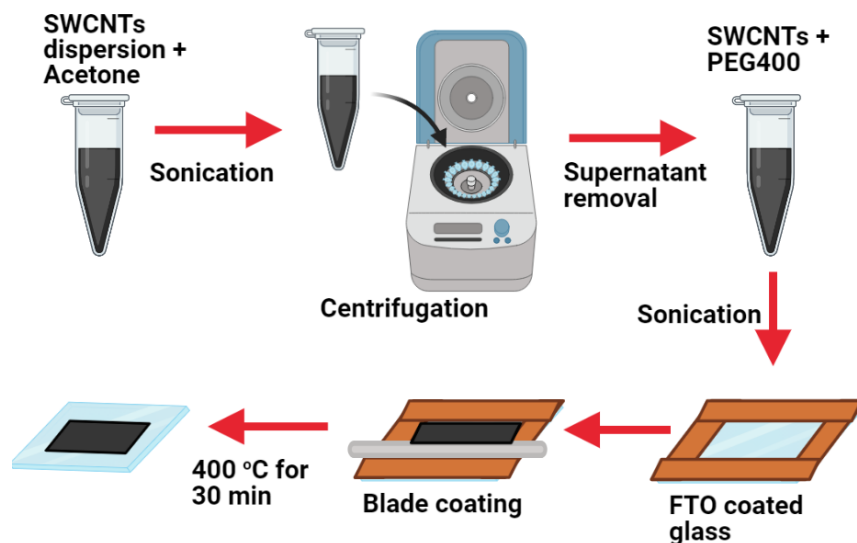
Figure 3.2: SWCNTs film deposition process on FTO coated glass. The starting solution dispersion of 0.04 wt.% SWCNTs with 1 wt.% of SDS was converted into a gel, blade coated and heated at 400 oC to remove the PEG from the gel.

For the film deposition onto the FTO conductive glass plates, rectangles of around $1cm^2$ were made using Kapton tape to limit the size and thickness of the film deposition. Then, some drops of the gel were spread in the substrate using a glass slide, and the films were allowed to dry at 200 ^oC for 60 minutes.

Finally, the films were heated at 400 ^oC for 30 minutes at a heating rate of 20$^oC/min$ to remove the PEG.

3.4.2   Candle soot film deposition

Candle soot corresponds to the residual black carbon particles generated during the burning of candles.[63] In order to collect the candle soot, fluorine-doped tin oxide (FTO) coated glass was put on the tip of the flame of a candle with the help of tongs. The resulting black film was directly used as a counter electrode in DSSCs.

3.5   Electrolyte preparation

Electrolyte solution was prepared by adding 0.1042 g of 0.5M potassium iodide (KI) and 0.0126 g of 0.05M metallic iodine (I) using polyethylene glycol (PEG) as solvent. The mixture was stirred for 10 minutes until obtaining an homogeneus solution of 3.24 mL. The prepared solution was stored in black bottle and was used as electrolyte.

3.6   DSSCs fabrication

The photoanodes were immersed in the dye solutions of mortiño and Jamaica for 90 minutes in order to let the TiO_2 adsorb the dye. At the same time, one of the photoanodes was left with a soaking time of 20 hours to study the effect of the sensitization time. The excess dye was removed by rinsing the photoanodes with ethanol. Then, a drop of electrolyte was spread over the photoelectrode, and it was clipped with the counter electrode to form a sandwich-type arrangement. Finally, the fabricated cells are illuminated under a light source calibrated with the standard AM 1.5G (100 $mWcm^{-1}$).

3.7   Sample preparation and characterization equipment

3.7.1   Raman spectroscopy

The Raman spectra were recorded using a HORIBA LabRAM HR Evolution Raman spectrometer (see Figure 3.3 part a)) with two lasers with excitation energies of 532 and 633 nm. Confocal Raman spectroscopy presents the ability to spatially filter the analysis volume of the sample, in the xy (lateral) and z (depth) axes.[64] Also, the integrated microscope allows a high magnification visualization of the sample and a microscopic laser spot. A schematic diagram of the Raman spectrometer used is present in Figure
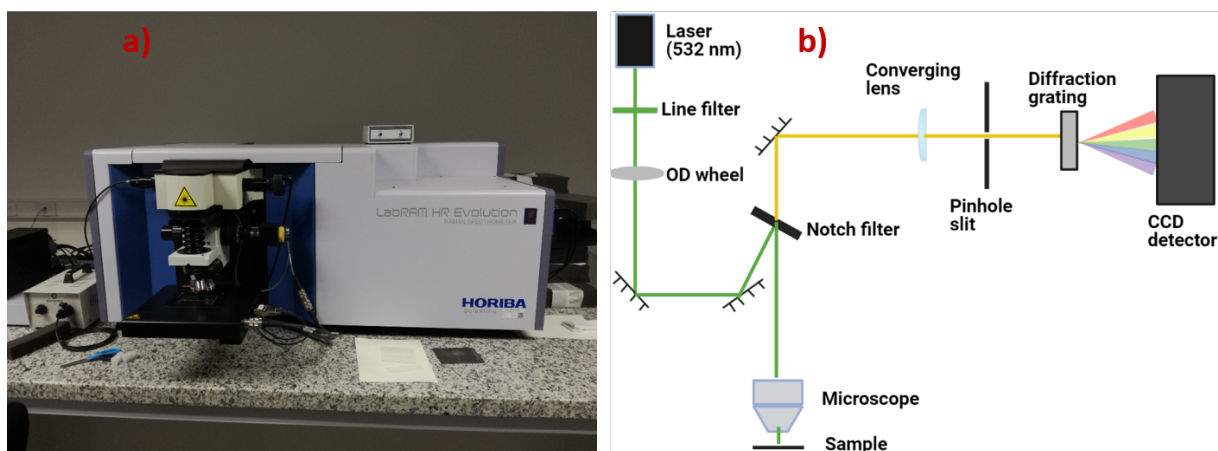
Figure 3.3: a) HORIBA LabRAM HR Evolution Raman spectrometer equipment and b) schematic diagram of the internal optics present in the Raman spectrometer.

3.3 part b), where the path of the 532 nm laser is shown. First, the laser line passes through a line filter to reduce the background plasma and secondary emissions. Then, it goes through the optical density (OD) wheel enabling power modifications, and is reflected to the microscope by the Notch filter. The laser line is focused through the objective (in this case x100 objective is used) from the microscope and hits the sample, where the scattered light returns along the same path as the incident light. As the notch filter is present, the Raman-shifted scattered photons pass through it and the converging lens focuses the light through a pinhole slit. At this point, an image of the sample is formed onto the pinhole with a magnification depending on the objective magnification used previously and the pinhole size limiting the collection of the signal to a region of the sample down to 1 μm. Finally, the light passes through the diffraction grating to split the light according to its wavelength and it is sent to the CCD detector.[65] The final Raman intensity of each spectral line is measured by counting the number of photons recorded for that line.[49]

The SWCNTs dispersion in SDS sample was prepared in a silicon wafer, where some drops of the solution were deposited and dried using a heating plate to form a film. The measurements were performed using the two lasers, but the results present only the measurements obtained with the 532 nm laser. Also, the measurements were performed using a 100x objective.

3.7.2   X-ray Diffraction

X-ray diffraction patterns were obtained using a Rigaku MiniFlex 600 XRD diffractometer (see Figure 3.4 part a)) with a D/teX Ultra2 detector. The measurement conditions were 40 kV and 15 mA. The scan range with a step wodth of 0.01^o. Powder samples were collected over double sided tape in an aluminium sample holder.
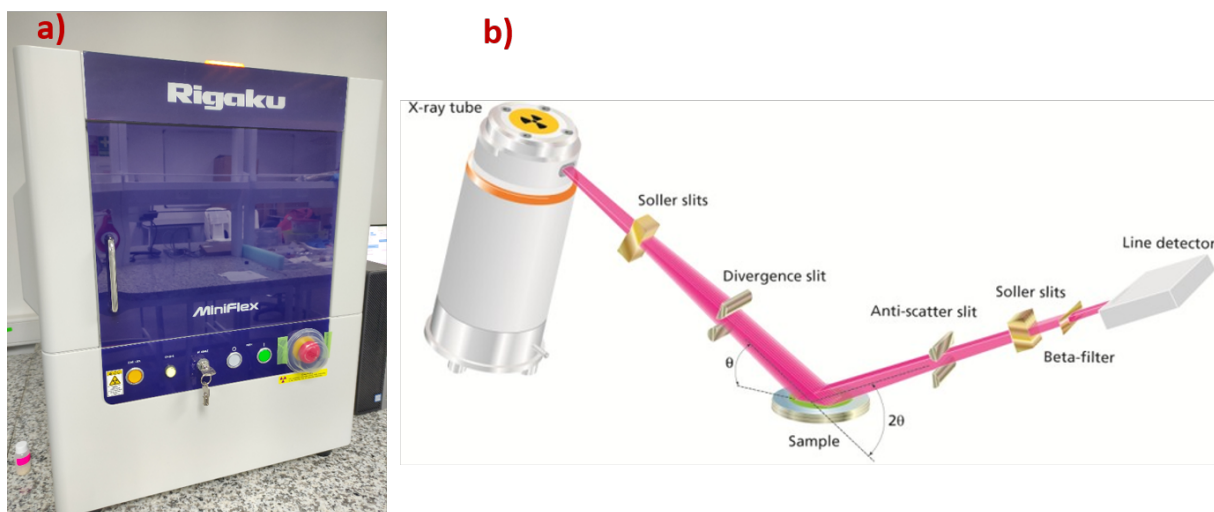
Figure 3.4: a) Rigaku MiniFlex 600 XRD diffractometer equipment and b) Schematic diagram of the XRD setup. Modified figure from Konig et al.[66]

A simplified X-ray diffractometer schematic setup can be observed in Figure 3.4 part b). It presents a ray tube to produce Cu K_α X-rays (λ=0.15406 nm), a spinning sample stage, and a line detector corresponding to a wide area scintillation counter detection system.[66] The X-rays are filtered, collimated, and directed to the sample and as the sample and detector are rotated 2θ angles, Bragg peaks are recorded in the detector.[53] It is important to mention that along the path of the X-rays and diffracted X-rays from the sample, there are several optics for optimizing the quality of the data output. Soller slits are important to limit the axial (cross or vertical) divergence of the incident and diffracted X-ray beams while the beta filter is important for data smoothing.[67]

3.7.3 UV-Vis spectroscopy

UV-Vis spectroscopy was performed in a Jenway Genova Nano Spectrophotometer (see Figure 3.5 part a)). The measurements were done using a path length of 0.2mm in the range of 200 to 800 nm. Before the measurements, the dye solutions were stored in the dark using aluminium foil to avoid photo-reactivity.
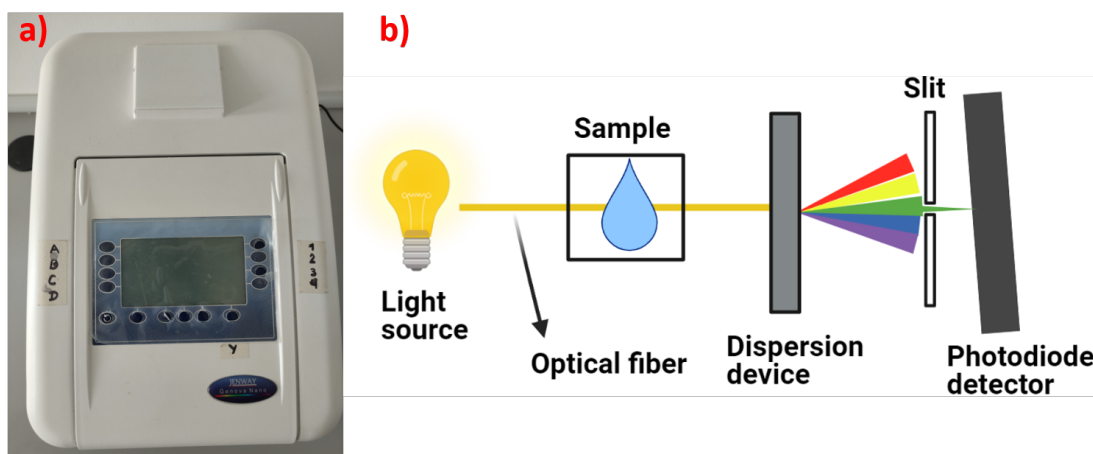
Figure 3.5: a) Jenway Genova Nano Spectrophotometer equipment and b) simple schematic diagram of the UV-Vis spectrometer optic array with a photodiode detector.

In Figure 3.5 part b) it is possible to observe the principal optic array of a UV-Vis spectrometer using a photodiode detector. In this case, the beam of light is transported through the fiber-optic and reaches the material sample. After collecting the light from the sample, a dispersive device as a diffraction grating is used to separate the light by wavelength. By using a slit, light of a certain wavelength reaches the photodiode detector.[42] It is important to mention that the Jenway Genova Nano Spectrophotometer has a fiber-optic, ultra-micro cell designed for measurements of extremely small sample volumes.

3.7.4 I-V curves

The fabricated cells are illuminated under a irradiation source composed by a 200 W lamp (81.9 V, 1.29 A in AC) and white LEDs arrangement calibrated under standard global AM 1.5 solar irradiation (100 $mWcm^{-2}$) by using a Peltier cell, see Figure 3.5. The I-V measurements were obtained using a bipolar power amplifier system with steps of 0.0012 V. An schematic diagram of the equipment can be seen Figure 1.8 and is detailed in Section 1.6.2.
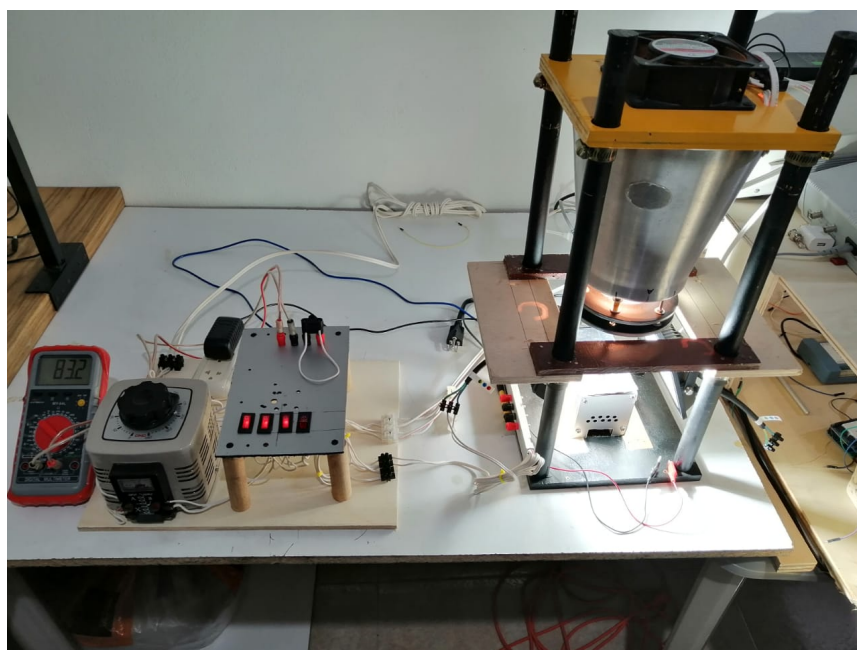
Figure 3.6: I-V curves measurement setup using a light source system calibrated under standard global AM 1.5 solar irradiation.

Chapter 4

Results & Discussion

4.1   UV-Vis absorbance of natural dyes

The UV-Vis absorption spectroscopy is used in this study to determine the range of optical absorption of the natural dyes extracted from mortiño and Jamaica flower. The UV-Vis absorption spectrums of the dye solutions of these plants extracted using ethanol as solvent are shown in Figure 4.1. The absorption peaks of mortiño and Jamaica flower dyes are present at 540 and 546 nm, respectively, which correspond to the presence of anthocyanin compounds. These compounds are known to exhibit a broadband absorption in the visible region with the maximum absorption spectrum ranging from 450 to 600 nm due to charge transfer transitions.[68] Both extracted dyes present a similar optical absorption range from 400 to 600 nm, even though they hardly absorb light in the red and near-infrared region. It is important to take into account that a wider absorbed spectrum ranges correspond with the conversion of more energy to electricity. Then, the spectrum in the red and near-infrared should be enhanced for a more efficient DSSC.

In the work of Ramirez J. et al.[20] it was found that the absorption peaks of rosella flowers (Hibiscus sabdariffa L.) and mortiño (accinium floribundum Kunt) extracts were about 520 and 536.5 nm, respectively. This shift in peak absorption compared to the present absorption spectrum can be attributed to the difference in pH of the ethanol extract solutions since this work uses an acidic pH of 1. It can be explained taking into account that anthocyanins are phenolic compounds that are pH-dependent, giving rise to different chemical species with different functional groups.[69] In a similar extraction process using ethanol as solvent without pH modifications, Suhaimi et al.[21] obtained an absorbance spectrum from flor de Jamaica with an absorption peak around 560 nm and a similar absorption range. It is important to mention that as the extracts from mortiño and flor de Jamaica were not purified, the presence of some impurities or particles
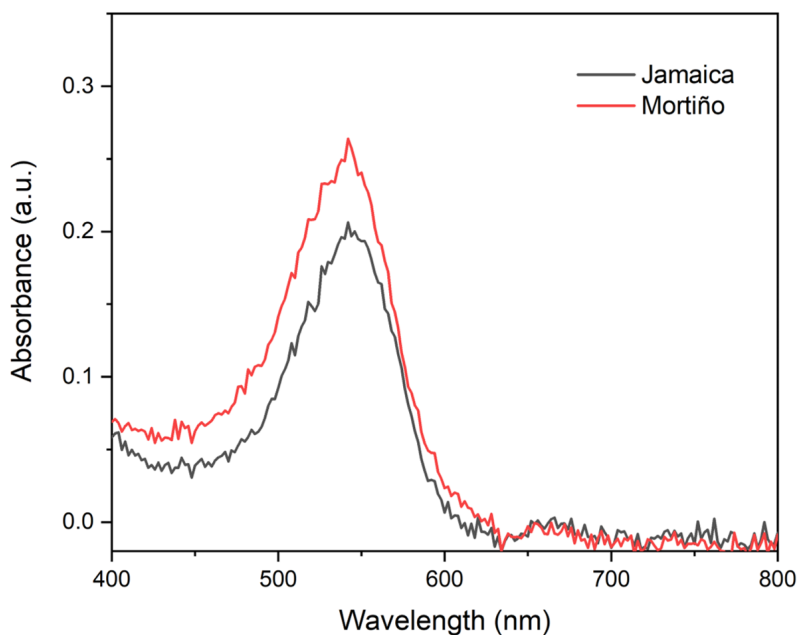
Figure 4.1: UV-Vis absorption spectrum from natural dyes: Jamaica flower in black and mortiño in red.

could be present causing little differences in the absorbance spectra. In general, the absorbance of mortiño and flor de Jamaica is comparable with other extractions present in literature.

4.2 Raman spectroscopy

4.2.1 SWCNTs dispersion and SWCNTs film

Raman spectroscopy was used in this study to identify if the film deposition process and the heat treatment at $400\ ^oC$ modifies the stability of the crystalline structure of the SWCNTs and their diameter distribution. The starting material is an aqueous solution dispersion of 0.04 wt. % SWCNTs with 1 wt.% of sodium dodecyl sulfate (SDS). For the Raman analysis, drops of the sample were dried over a silicon wafer using a heating plate. The Raman spectrum from the SWCNTs dispersion was obtained by using a 532 nm (2.33 eV) excitation laser from $100\ cm^{-1}$ to $3000\ cm^{-1}$ and averaging the measurements of three different points of the sample. Figure 4.2 shows the normalized Raman spectrum with four dominant Raman features for the SWCNTs dispersion: the radial breathing mode (RBM) at low frequencies, the tangential G-band, the dispersive disorder induced D-band, and the G' band at high frequencies.
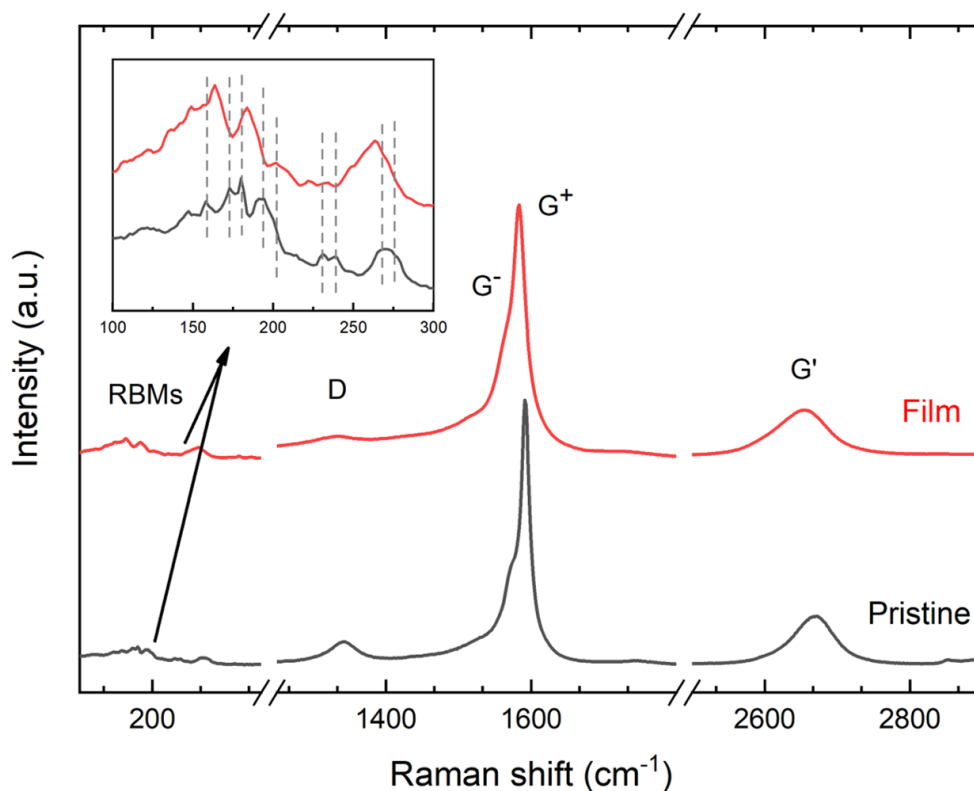
Figure 4.2: Normalized Raman spectrum of pristine SWCNTs dispersed in aqueous solution with 1 wt.% of SDS (black) and SWCNTs film deposited over the conductive glass (red). The inset shows the RBMs peaks of both samples.

The G-band corresponds to tangential modes, which predominantly involves the sp^2 inplane carbon-carbon bonds and depends strongly on the metal or semiconducting nature of the tube and changes in the Fermi level. Also, this band is characteristic of highly ordered carbon species[49,70]. It is possible to observe the presence of a shoulder in the G-band corresponding to the splitting into the G^- and G^+ peaks at 1583.06 and 1592.51 cm^{-1}. The G^- feature is broad and asymmetric, which can be represented by the Breit–Wigner–Fano (BWF) line shape and is attributed to a metallic behavior of the carbon nanotubes. This line shape occurs when lattice vibration couples to free electrons when an electron-phonon interaction takes place.[49] The D and G' features corresponding to one- and two-phonon, second-order Raman scattering processes are present at 1342.35 and 2671.81 cm^{-1} respectively. The D-band or disorder band arises from structural defects in the nanotube wall[25]. Then, the ratio of the intensities of the disorder-induced D-band

to the G-band ratio (I_D/I_G) is commonly used to characterize the disorder in carbon nanotube samples[71], which in this case is equal to 0.0932.

In Figure 4.2 it is also possible to observe the Raman spectra of the gel-coated binder-free SWCNTs film on conductive glass obtained after removing the excess of SDS from the SWCNTs dispersion and the PEG from the SWCNTs gel by heating at 400 ^oC. In this case, the I_D/I_G ratio corresponds to a value of 0.1313, which means that the heat treatment does not introduce defects in the crystalline structure of the SWCNTs. The defect related D-band is located at 1335.91 cm^{-1} and the two main G modes signals G^- and G^+ at 1583.37 and 1567.01 cm^{-1} respectively. These positions present slightly shifts to lower frequency values compared to the SWCNTs dispersion that can be attributed to the exposure of the SWCNTs to a temperature of 400^oC.[72]

Also, the double peak structure of the G-band presents a significant broadening compared to SWCNTs dispersion. By fitting the low frequency (G^-) feature with the Breit-Wigner-Fano (BWF) lineshape and the high frequency (G^+) feature with a Lorentzian lineshape, it is possible to analyze the full width at half maximum (FWHM) of the peaks in both samples. Compared to the SWCNTs dispersion with a FWHM of 47.55 and 12.16 cm^{-1} for G^- and G^+ peaks, the FWHM in the SWCNTs film are of 56.26 and 24.09 cm^{-1} respectively. This increase in FWHM is attributed to a lower concentration of SDS obtained after the film deposition process. This result is in accordance with the work of Rossi J. et al.[62], which attributes the reduction in FWHM of SWCNTs G peak to SDS exposure and suppression of the BFW lineshape in the presence of the surfactant, which indicates that the SDS acts as a SWCNT dopant. Likewise, the Raman G' peak position of the SWCNTs is sensitive to the presence of SDS, which manifests as a downshift in frequency of around 15.53 cm^{-1} in the SWCNTs film compared to the SDS dispersion. Then, the film deposition process did not involve an strong doping in the SWCNTs after dispersing them in PEG and their removal with the heat treatment.

The black line inset in Figure 4.2 shows in the low-energy range from $100cm^{-1}$ to $300cm^{-1}$ several peaks in the SWCNTs dispersion solution resulting from the radial breathing modes of the resonantly excited tubes. The RBM peaks were fitted using a sum of nine Lorentzian lineshapes as can be seen in Figure 4.3 part a), and the most intense peaks are around 181.41, 172.32, 192,31 and 200.03 cm^{-1}. The high number of peaks at different frequencies corresponds to a diameter distribution of different SWCNTs in resonance at this laser excitation energy, which suggests a large number of (n, m) chirality's present in the sample.

In the case of the deposited SWCNTs film over the FTO conductive glass, the red line inset in Figure 4.2 shows a similar RBM peak pattern compared to the SWCNTs dispersion. The RBM peaks were fitted using a sum of nine Lorentzian lineshapes, as can be seen in Figure 4.3 part b). The peaks correspond
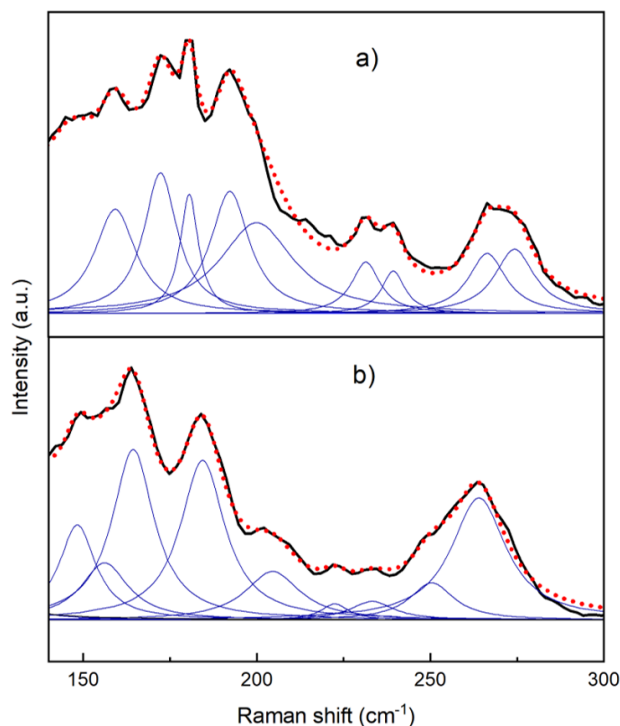
Figure 4.3: RBM fittings of a) SWCNTs dispersed in aqueous solution with 1 wt. % of SDS and b) SWCNTs film deposited over the conductive glass. Both fittings were performed using nine Lorentzians.

to almost the same SWCNTs population from the dispersion. These peaks present a small shift to lower frequencies that varies from 6.17 to 10.34 cm^{-1}, which is caused by different environmental effects as the bundle organization and inter-nanotube contact area changes after the film deposition process. This can be explained as an aggregation effect from the dispersion and the solid film, which shifts the effective excitation profile and causes peaks to increase or decrease, depending on where the transition lies relative to the excitation wavelength.[73] In general, Raman spectroscopy showed that structural defects were not introduced during the film deposition process of SWCNTs and that PEG was successfully removed. This corresponds to a good result as the presence of structural defects or PEG in the counter electrode could affect the conductivity, catalytic properties and surface area of the SWCNTs. The reason behind the need to remove the PEG is because inert binders, as polymers, can lower the catalytic and conductive capabilities of the SWCNT film since they reduce the contact area between CNTs and electrolyte and block the inter-nanotube charge transport.[74]

Sample	ω_{RBM} (cm^{-1})	Reference ω_{RBM} (cm^{-1})	Reference d(Å)	Assigned chirality	S/M	Chirality from Strano et. al.	Chirality from Fantini et. al.
SWCNTs Dispersion	172.32	174.5	**1.34**	**(14,5)**	M	(13,7)	-
	181.41	182	**1.29**	**(16,1)**	M	(16,1)	(11,8)
	192.31	193.5	**1.21**	**(13,4)**	M	(13,4)	(12,6)
	200.03	200.4	**1.18**	**(15,0)**	M	(15,0)	(14,2)
	231.47	230.8	**1.02**	**(13,0)**	S	(9,6)	(11,3)
	239.38	238	**0.98**	**(10,4)**	M	(10,4)	(10,4)
	266.43	266.7	**0.86**	**(11,0)**	S	(8,5)	(8,5)
	274.30	272.7	**0.85**	**(9,3)**	M	(9,3)	(9,3)
	159.27	-	-	-	-	-	-

Table 4.1: Assignment of SWCNTs chirality and diameter from RBM frequencies in aqueous solution dispersion. The work of Maultzsch,et al. [75] about chiral index assignment was used as reference and work of Strano [76] and Fantini [77] for chirality assignment comparison.

For the assignment of the RBM frequencies from the SWCNTs dispersion and films, fittings of the resonance profiles in the range of 140 to 350 cm^{-1} were performed, which can be seen in Figure 4.3. The assignment of these frequencies to a particular tube chirality (n, m) was performed using the work of Maultzsch et al. [75] as reference, which presents a sample containing SDS as surfactant. For this, each peak frequency was compared to the experimental frequencies found in Table 1 and 2 from her study, and the closest was assigned to its chirality. In Table 4.1 the first column represents the peak frequencies measured, while the second column shows the closest frequencies from Maultzsch work. The assigned chirality, tube diameter, and electric type are also present in Table 4.1. Also, the assigned chiralities were compared with the works of Strano [76], and Fantini [77], which assignment can be seen in the last two columns of Table 4.1. It should be noted that many of the assignments are in agreement when comparing the references.

The effect of the environment of the tubes, as the presence of SDS, on the RBM frequency and the optical transition energies of the SWCNTs should be discussed. The aggregation state of SWCNTs bundles in the solid-state presents an effect in the RBM frequency distribution. [78] Studies in the determination of optical transition energies (E_{ii}) has shown that SDS wrapped isolated SWNTs in aqueous solution exhibit a blueshift (~70 meV) with respect to bundled SWCNTs. Then, in unbundling process as an SDS dispersion, the values for E_{ii} will blueshift, resulting in a change of the relative intensities of the RBMs. [77] In the

work of Cardenas et al.[79] the distribution of RBMs in SWNCTs dispersion solution using SDBS is shifted to lower frequencies in comparison to the one using SDS as surfactant. This effect may be accounted to a higher dielectric constant (due to anionic character) in the presence of SDBS and a better unbundle mechanism in comparison to the SDS dispersion. Then, an increase in transition energy is present resulting in larger diameter tubes coming into resonance and consequently. In a similar way, Izard et al.[80] studied the RBM features coming from bundled tubes to bundles wrapped by SDS and to individual tubes in SDS. They observed that the metallic tubes were more sensitive to the surfactant and present a larger RBM upshift in comparison to semiconducting tubes due to small changes in the resonance condition. It is important to mention the Maultzsch et al.[75] stated that the assignments performed in their work are not affected by the surfactant-induced variation in the transition energies and RBM frequencies.

Taking that into account, in order to fully determine the chiralities of a SWCNTs sample, using Raman spectroscopy, it is necessary to use various lasers with different excitation energies in order to excite the transition or resonance energy (E_{ii}) from each nanotube chirality. Therefore, in this study, it is not possible to conclude the chiralities and diameters of SWCNTs present. However, a good amount of the assigned chiralities may be present in this case.

4.2.2 Candle soot film

In the case of the candle soot film, the Raman spectra was recorded over the conductive glass as substrate with a 532 nm (2.33 eV) excitation laser from 100 cm^{-1} to 3000 cm^{-1}. According to Zhang et al.[52], generally the candle soot is constituted of regular and small carbon nanoparticles (20–50 nm). In Figure 4.4 two broad and overlapping peaks are present. The first one corresponds to the D-band with a peak at 1337.5 cm^{-1}, which is a characteristic feature of amorphous carbon[81]. The peak at 1597.08 cm^{-1} from the G-band corresponds to E_{2g} mode of graphite due to the vibration of sp^2-bonded carbon atoms in a 2D hexagonal lattice[81]. This G-band indicates the presence of graphitic carbon in the candle soot. The ratio of intensities of D-band to G-band proportional (I_D/I_G) to the structural disorder in the samples is equal to 0.97. At higher frequencies, the soot sample exhibits broad signals in the range of about 2300 cm^{-1} to 3000 cm^{-1} (Figure 4.4) that can be attributed to second-order bands, i.e., overtones and combinations of graphitic lattice vibration modes.[82] Then, Raman spectra of soot can be interpreted in terms of highly disordered graphitic structures.

The Raman spectra from the candle soot film is comparable to the work of Gangadharan et al.[83] where candle soot was also collected on a stainless-steel substrate and the corresponding Raman spectra presents the characteristic D and G peaks at 1340 cm^{-1} and 1540 cm^{-1}, respectively. They obtained an ID/IG ratio of 0.97, which is the same of our work. In the same way, Kakunuri et al.[84] deposited candle soot from the
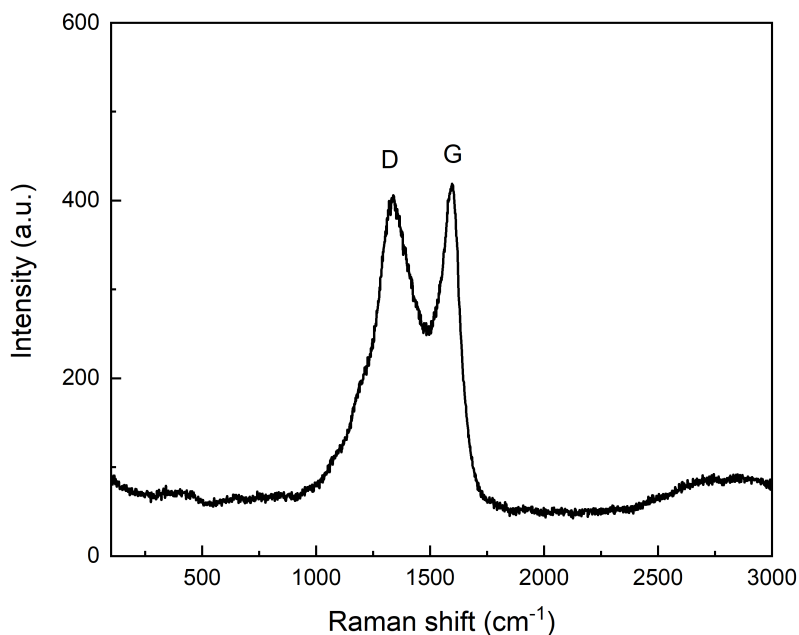
Figure 4.4: Raman spectrum of candle soot deposited on conductive glass taken with a 532 nm laser. Characteristic D-band and G-band peaks are present corresponding to highly disordered graphitic particles.

tip of the flame presents a similar Raman spectrum.

4.3   Titanium dioxide X-ray diffraction

The crystal structure of commercial TiO_2 powder from LOBAChemie and TiO_2 film deposited as photoanode material were examined by using XRD analysis. Figure 4.5 illustrate the XRD patterns, which determines the presence of the anatase and rutile phases of TiO_2. It follows that for both samples, the high intensity peaks at around $2\theta = 25.47^o$, 37.96^o, 48.27^o, 54.12^o, 55.34^o, 62.87^o and 75.27^o, corresponding to the (101), (004), (200), (105), (211), (204) and (215) planes indicate the crystalline anatase structure. The lower intensity crystal peaks at around $2\theta = 27.58^o$, 36.30^o, and 69.19^o, corresponding to the (110), (101), and (301) planes indicate the rutile structure. This XRD structure was confirmed with the Joint Committee on Powder Diffraction Standards[85], TiO_2 anatase (JCPDS card no. 21-1272) and TiO_2 rutile (JCPDS card no. 21-1276) structure. It is important to mention that the anatase phase presents high surface area, high coefficient of electron diffusion, and low dielectric constant, which is considered an ideal candidate
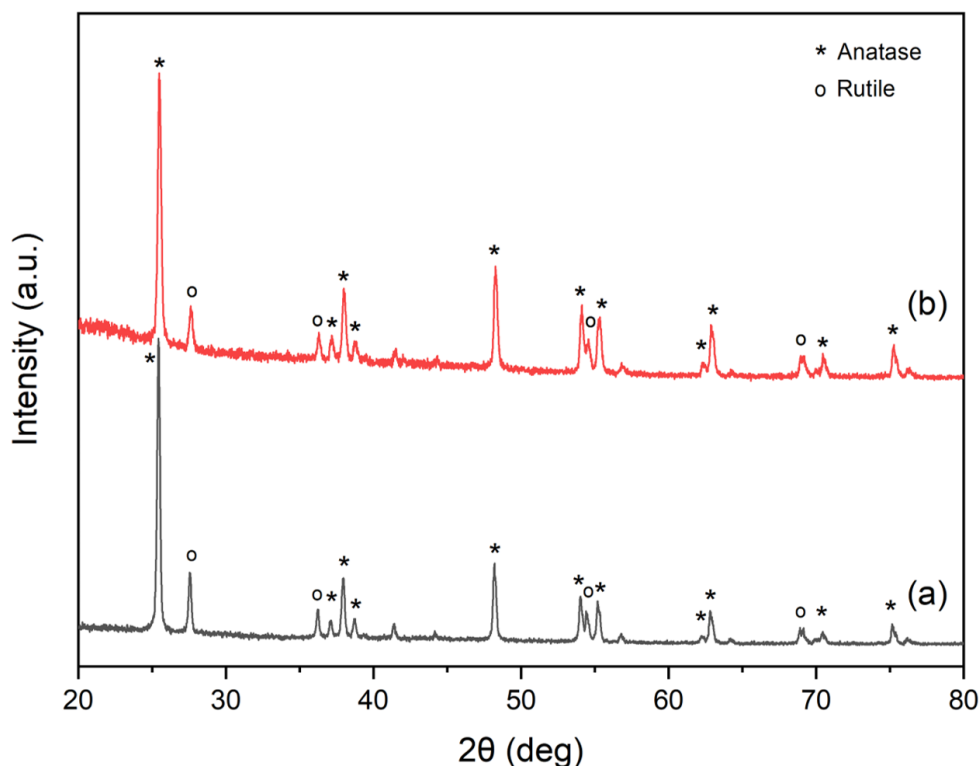
Figure 4.5: X-ray diffraction patterns of (a) commercial TiO_2 powder from LOBAChemie and (b) TiO_2 powder collected from the photoanode film after sintering treatment at $450\,^oC$. Symbols $*$ and ^{o} corresponds to the anatase and rutile TiO_2 phases respectively.

compared to rutile.[10] In Figure 4.5 it can be noted that the rutile phase peaks present a slight decrease in intensity compared to the anatase phase peaks after the sintering process at 450^oC in the film deposition process. By using WPPF (Whole Powder Pattern Fitting) analysis method in the commercial TiO_2 powder sample, the weight fraction of anatase is 78.9 % and for rutile is 21.1 %. In the case of the sintered film, the weight fraction of anatase is 83.5 % and for rutile is 16.5 %. Also, XRD spectra from the TiO_2 film does not show the presence of the PEG and the acetic acid use during the preparation of photoelectrodes. As expected only TiO_2 particles remain in the photoanode film for later use in a DSSC.

4.4   Photovoltaic performance

A light source system calibrated under standard global AM 1.5 solar irradiation composed of a 200 W lamp (81.9 V, 1.29 A in AC) and white LEDs (20 W) arrangement was used for testing the fabricated DSSCs. The spectrum from the light source system can be seen in Figure 4.6, which was measured in the range of 300 to 770 nm with a Thunder Optics SMA-E Spectrometer. The spectrum is comparable to the ASTM G-173-03 spectra corresponding to the global total spectral irradiance between the measured wavelength range.
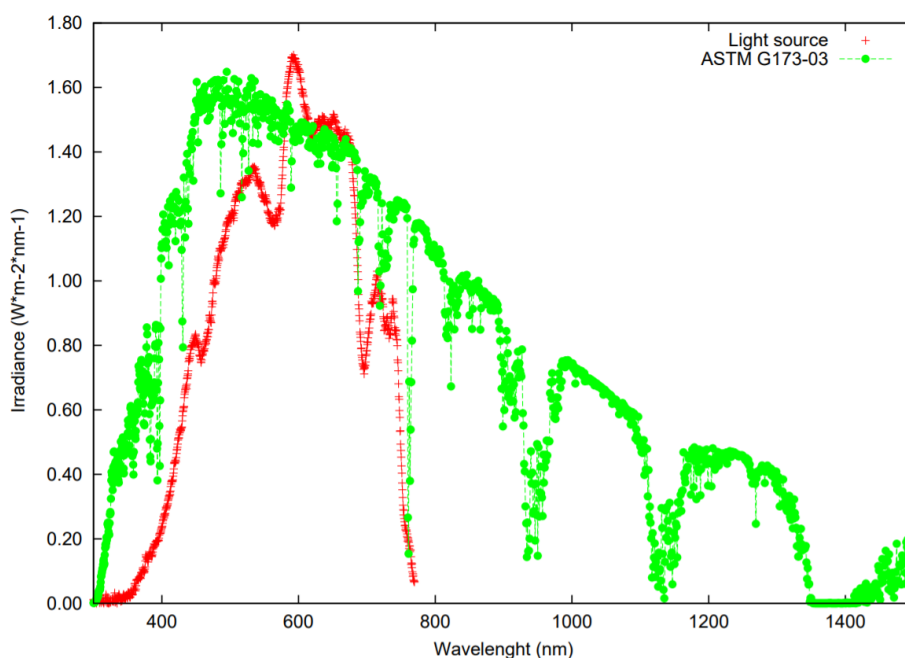
Figure 4.6: Comparison between the terrestrial solar spectra under standard global AM 1.5 solar irradiation (represented by ASTM G-173-03 spectra) in green and our light source system in red measured from 300 to 770 nm.

From the current density-voltage curves of the fabricated DSSCs, the overall performance of natural dyes as sensitizers and counter electrode films was evaluated in terms of open-circuit voltage (V_{oc}), short-circuit current (J_{sc}), maximum power output (P_{max}), fill factor (FF), and power conversion efficiency (η). Figure 4.7 shows the current density-voltage curves of four DSSCs fabricated using mortiño and Jamaica flower dyes as sensitizers (with TiO_2 film soaking time of 90 minutes), while SWCNTs and candle soot

films are used as counter electrodes. The fill factors and power conversion efficiencies of these cells varied from 29 to 36 % and 0.0003 to 0.0053 %, respectively. The P_{max} values varied from 2.9×10^{-5} to 7×10^{-4} $mWcm^{-2}$.
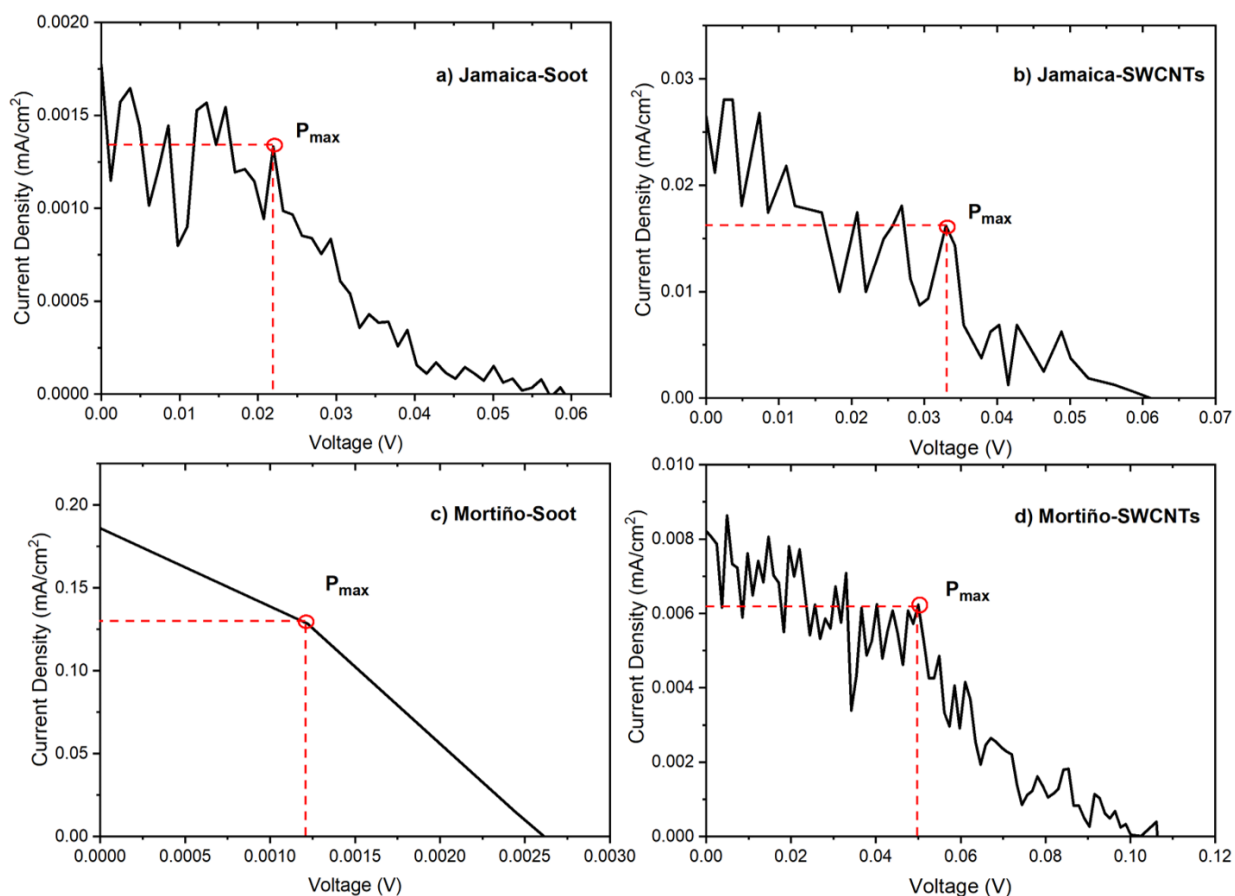
Figure 4.7: Current-voltage curves of the DSSCs with a) Jamaica flower dye as sensitizer and candle soot film as counter electrode, b) Jamaica flower dye as sensitizer and SWCNTs film as counter electrode, c) mortiño dye as sensitizer and candle soot film as counter electrode, d) mortiño dye as sensitizer and SWCNTs film as counter electrode. The sensitization time (soaking time) of the TiO_2 films with the dyes were of 90 minutes. Points of maximum power output (P_{max}) are highlighted in each curve.

The higher FFs, power conversion efficiencies, and P_{max} values corresponds to cells using SWCNTs film as counter electrode, which can be attributed to a low charge transfer resistance and a better electrocatalytic activity of the SWCNTs coupled to a higher surface area[30] compared with the candle soot film. As the

electrochemical catalysis is proportional to the contact area between the electrode and the electrolyte[30], DSSCs with SWCNTs film present a better performance. Unlike the work of Mei X. et al.[30], which used a similar SWCNTs gel deposition process, the SWCNTs films did not present a good adhesion to the substrate and started to detach after the heating process at 400^oC and in contact with the electrolyte, as can be seen in Figure 4.8. This effect could lower the charge transport at the interface between the electrolyte and the counter electrode due to the cracks in the SWCNTs film. Although the heating process to 400^oC removed the PEG binder and did not introduce defects on the crystalline structure of the SWCNTs in the film deposition methodology (according to the Raman spectroscopy results), the adhesion of the film to the substrate should be enhanced.
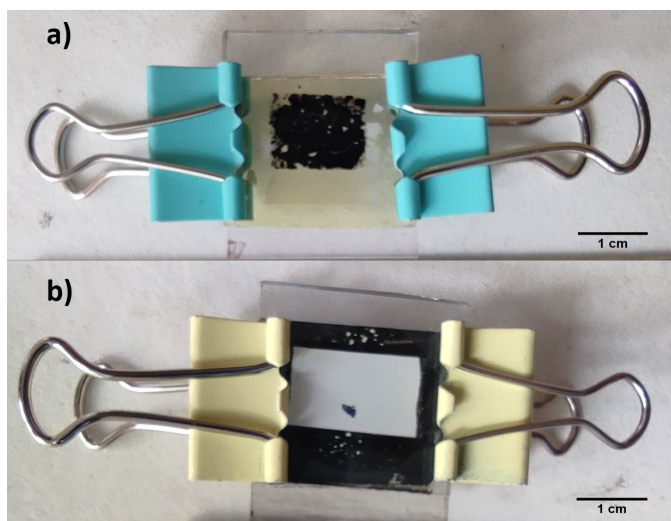
Figure 4.8: DSSCs fabricated using a) SWCNTs film counter electrode and b) candle soot in the counter electrode. In the case of the SWCNTs film, it started to detach from the FTO conductive glass substrate after the heat treatment at 400 ^oC.

Despite the presence of anthocyanins in both extractions of the two natural dyes, different anthocyanin compounds and quantities lead to different η values in the fabricated DSSCs. A different dye structure affects the chemical attachment of the dye to the TiO_2 film and the energy levels of the highest occupied molecular level (HOMO) and the dye molecule's lowest unoccupied molecular level (LUMO).[68] Also, the interaction between the energy levels of the redox potential of the electrolyte and the HOMO of the dye should be different for each dye extraction composition. Many studies determined that the J_{sc} value present a significant influence on the absorption capability of the vegetable dyes.[86] At higher absorption

Cell (Dye-Counter electrode)	Area ± 0.01 (cm^2)	V_{oc} ± 0.001 (V)	J_{sc} ($mAcm^{-2}$)	P_{max} ($mWcm^{-2}$)	FF (%)	η (%)
Jamaica-SWCNTs	0.74	0.061	0.0265 ± 0.0008	5.3×10^{-4} $\pm 3 \times 10^{-5}$	33 ± 1	0.0053 ± 0.0003
Jamaica-Soot	1.91	0.059	0.0017 ± 0.0003	2.9×10^{-5} $\pm 6 \times 10^{-6}$	29 ± 4	0.0003 $\pm 6 \times 10^{-5}$
Mortiño-SWCNTs	0.84	0.106	0.0082 ± 0.0006	3.1×10^{-4} $\pm 3 \times 10^{-5}$	36 ± 3	0.0031 ± 0.0003
Mortiño-Soot	1.54	0.003	0.1861 ± 0.001	2×10^{-4} $\pm 2 \times 10^{-4}$	31 ± 15	0.002 ± 0.001
Mortiño-Soot (sensitized 20h)	1.43	0.440	0.0044 ± 0.0003	7×10^{-4} $\pm 1 \times 10^{-4}$	34 ± 3	0.0066 ± 0.0007

Table 4.2: Active area and photovoltaic parameters of DSSCs based on mortiño and Jamaica flower sensitizers using a SWCNTs or candle soot film at the counter electrode. The TiO_2 layer of the first four cells in the table was soaked in the natural dye for 90 minutes, while the TiO_2 layer of the last cell in the table was soaked in the natural dye for 20 hours.

capability, higher the J_{sc} of a DSSC will be. In the study of Ramirez-Perez et al.[20] it was determined that the ability to absorb light was higher for the dye extracted from Mortiño fruit than for those from Jamaica flowers by examining the J_sc values. However, in this work is not possible to determine which extracted dye present a better performance in the fabricated DSSCs.

Table 4.2 summarizes the photovoltaic parameters of the different cells. In general, the maximum power output P_{max} (dependent of the V_{oc} and J_{sc} values) and power conversion efficiency values are low. The main reason could be due to the low spectral response of the sensitized TiO_2 under light excitation. In this case, TiO_2 commercial powder (large particle size) is used to form the paste deposited over the conductive glass. Instead, small TiO_2 nanoparticles should be used as the smaller particle size of TiO_2 present a higher surface area, the number of adsorbed dyes anchored to the TiO_2 film increases, and back-scattering light is reduced.[68] Also, the packing and porosity coming from TiO_2 small nanoparticle size results in a higher electrolyte penetration. A greater number of pores in the TiO_2 film could enhance the regeneration of the oxidized dye and the charge transport.[87] Furthermore, another potential reason for the small efficiencies was the lack of control of the TiO_2 film thickness.

It is important to mention that in Table 4.2 the differences in area from each fabricated DSSC arrives
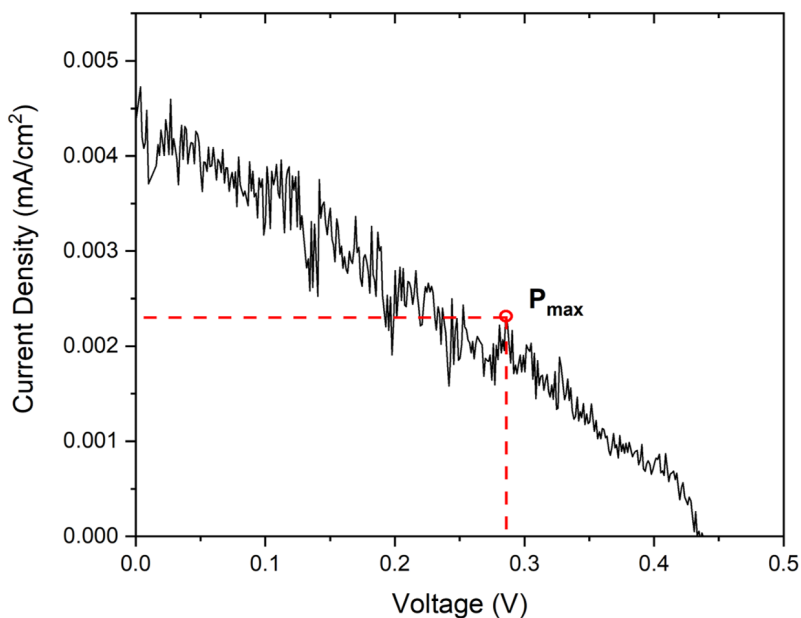
Figure 4.9: Current-voltage curve for the DSSC sensitized using mortiño dye with a soaking time of 20 hours and candle soot film as counter electrode. Point of maximum power output (*Pmax*) are highlighted in the curve.

from the bad control of the SWCNTs and candle soot films size deposited on the FTO conductive glass. As a consequence, when joining the photoanode with the counter electrode in the DSSC fabrication, the contact area between the SWCNTs and candle soot films varied between each cell. Although the areas are different, this does not represent a problem since the calculated power conversion efficiencies are independent on the area.

The effect of the sensitization time on the performance of a DSSC was studied by using a different soaking time of the TiO_2 layer on the mortiño dye sensitizer. This corresponds to an important parameter to take into account since different dye sensitized materials have different adsorption rates, and the sensitization time governs the amount of dye to be adsorbed onto the TiO_2 particles.[88] Figure 4.9 shows the current density-voltage curve of a DSSCs using mortiño dye as sensitizer with a sensitization time of 20 hours and carbon soot as counter electrode. The power conversion efficiency and maximum power output values of this DSSC increased from 0.002 to 0.0066 % and $2x10^{-4}$ to $7x10^{-4}$ $mWcm^{-2}$ respectively, compared with the same DSSC sensitized for 90 minutes. Moreover, the power conversion efficiency of this DSSC is the highest among all the others, as can be seen in Figure 4.10, where η of all the fabricated
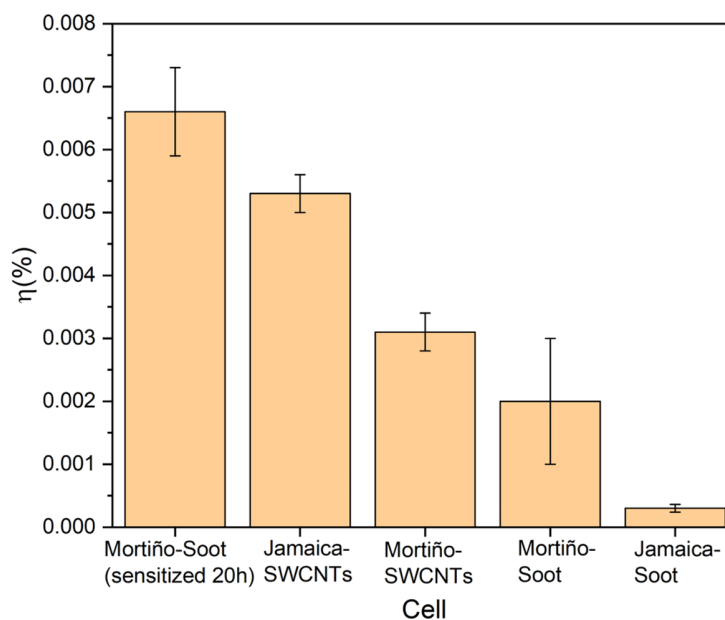
Figure 4.10: Comparison bar graph of power conversion efficiency (η) values from the different fabricated DSSCs. Cells are labelled based on their components as dye sensitizer-counter electrode.

cells are shown. The higher sensitization time of the TiO_2 film with the natural dye is a remarkable factor enhancing the anchoring between the dye molecules and the TiO_2 particles. This could produce a better electron injection between the LUMO energy level of the anthocyanins in the dyes and the conduction band of the TiO_2.[43] As a result, the spectral response of TiO_2 to visible light is enhanced due to a higher amount of natural dye molecules and their photoactive activity.

Chapter 5

Conclusions & Outlook

In this work, dye sensitized solar cells using natural dyes extracted from mortiño (Vaccinium floribundum Kunth) and Jamaica flower (Hibiscus sabdariffa L.) with SWCNTs and carbon soot films as counter electrodes were fabricated. The dye extraction using ethanol as solvent presented an optical absorption band in the visible range from 400 to 600 nm due to the presence of anthocyanin molecules as the main dye component, which is important to enhance the spectral response of the TiO_2 film to visible light. In the case of the SWCNTs counter electrode, Raman spectroscopy results revealed that the film deposition process and the heat treatment at 400^oC do not introduce defects in the crystalline structure of the SWCNTs by comparing the I_D/I_G ratio in the dispersion and the deposited film. The fittings of the RBM region of the Raman spectra in the dispersion and film samples correspond to almost the same population of SWCNTs. Moreover, the heating process successfully removed the PEG binder. X-ray diffraction measurements showed an increase in weight fraction of 4.6% of the anatase crystalline phase of TiO_2 at the photoanode after the heat treatment at 450^oC.

The photovoltaic measurements revealed that among the DSSCs with a soaking time of 90 min of the TiO_2 in the natural dyes, the highest maximum power output (P_{max}), filling factor (FF), and power conversion efficiency (η) values correspond to cells using the SWCNTs counter electrode. They showed a η of 0.0053 and a FF of 33 % for the cell sensitized with Jamaica, and a η of 0.0031 and a FF of 36 % for the cell sensitized with mortiño. This result is related to a low charge transfer resistance and a better electrocatalytic activity of the SWCNTs coupled to a higher surface area. Moreover, a higher sensitization time (20 hours) on the TiO_2 film of the cell fabricated with carbon soot as counter electrode and mortiño dye as sensitizer improved the P_{max} and η values to $7x10^{-4}$ $mWcm^{-2}$ and 0.0066 % respectively. This corresponds to the fabricated DSSC with higher photovoltaic performance, attributed to a better anchoring

between the dye molecules and the TiO_2 particles. In general, the fabricated DSSCs presented low P_{max} and η values compared to others present in literature. It is related, mainly, to low spectral response of the sensitized TiO_2 under light excitation from a too large particle size instead of nanostructured TiO_2.

Further work is required in order to fully determine the most efficient sensitization time for each natural dye, as different anthocyanin dye structures present different adsorption rates. Optical absorption properties of the TiO_2 after dye adsorption should be studied in order to determine the spectral response to visible light from the linking of the dye with the semiconductor. Furthermore, the adhesion of the SWCNTs film to the conductive glass substrate should be enhanced by modifying the temperature at which the PEG is removed from the film without causing crackings on it.

Bibliography

[1] Wu, J.; Lan, Z.; Lin, J.; Huang, M.; Huang, Y.; Fan, L.; Luo, G.; Lin, Y.; Xie, Y.; Wei, Y. Counter electrodes in dye-sensitized solar cells. *Chemical Society Reviews* **2017**, *46*, 5975–6023.

[2] Schiermeier, Q.; Tollefson, J.; Scully, T.; Witze, A.; Morton, O. Energy alternatives: Electricity without carbon. *Nature News* **2008**, *454*, 816–823.

[3] Ludin, N. A.; Al-Alwani Mahmoud, A. M.; Bakar Mohamad, A.; Kadhum, A. A. H.; Sopian, K.; Abdul Karim, N. S. Review on the development of natural dye photosensitizer for dye-sensitized solar cells. *Renewable and Sustainable Energy Reviews* **2014**, *31*, 386–396.

[4] Wu, J.; Lan, Z.; Lin, J.; Huang, M.; Huang, Y.; Fan, L.; Luo, G. Electrolytes in dye-sensitized solar cells. *Chemical Reviews* **2015**, *115*, 2136–2173.

[5] Mariotti, N.; Bonomo, M.; Fagiolari, L.; Barbero, N.; Gerbaldi, C.; Bella, F.; Barolo, C. Recent advances in eco-friendly and cost-effective materials towards sustainable dye-sensitized solar cells. *Green Chemistry* **2020**,

[6] Hug, H.; Bader, M.; Mair, P.; Glatzel, T. Biophotovoltaics: Natural pigments in dye-sensitized solar cells. *Applied Energy* **2014**, *115*, 216–225.

[7] O'regan, B.; Grätzel, M. A low-cost, high-efficiency solar cell based on dye-sensitized colloidal TiO 2 films. *nature* **1991**, *353*, 737–740.

[8] Kumara, N. T.; Lim, A.; Lim, C. M.; Petra, M. I.; Ekanayake, P. Recent progress and utilization of natural pigments in dye sensitized solar cells: A review. *Renewable and Sustainable Energy Reviews* **2017**, *78*, 301–317.

[9] Yu, H.; Zhang, B.; Chen, X.; Qian, X.; Jiang, D.; Wu, Q.; Wang, J.; Xu, J.; Su, L. Color-tunable visible photoluminescence of Eu: CaF 2 single crystals: variations of valence state and local lattice environment of Eu ions. *Optics Express* **2019**, *27*, 523–532.

[10] Karim, N. A.; Mehmood, U.; Zahid, H. F.; Asif, T. Nanostructured photoanode and counter electrode materials for efficient Dye-Sensitized Solar Cells (DSSCs). *Solar Energy* **2019**, *185*, 165–188.

[11] Tański, T.; Jarka, P.; Szindler, M.; Drygała, A.; Matysiak, W.; Libera, M. Study of dye sensitized solar cells photoelectrodes consisting of nanostructures. *Applied Surface Science* **2019**, *491*, 807–813.

[12] Babar, F.; Mehmood, U.; Asghar, H.; Mehdi, M. H.; Khan, A. U. H.; Khalid, H.; ul Huda, N.; Fatima, Z. Nanostructured photoanode materials and their deposition methods for efficient and economical third generation dye-sensitized solar cells: A comprehensive review. *Renewable and Sustainable Energy Reviews* **2020**, *129*, 109919.

[13] Hagfeldt, A.; Boschloo, G.; Sun, L.; Kloo, L.; Pettersson, H. Dye-sensitized solar cells. *Chemical reviews* **2010**, *110*, 6595–6663.

[14] Omar, A.; Ali, M. S.; Abd Rahim, N. Electron transport properties analysis of titanium dioxide dye-sensitized solar cells (TiO2-DSSCs) based natural dyes using electrochemical impedance spectroscopy concept: A review. *Solar Energy* **2020**, *207*, 1088–1121.

[15] Ooyama, Y.; Harima, Y. Photophysical and electrochemical properties, and molecular structures of organic dyes for dye-sensitized solar cells. *ChemPhysChem* **2012**, *13*, 4032–4080.

[16] Hemmatzadeh, R.; Jamali, A. Enhancing the optical absorption of anthocyanins for dye-sensitized solar cells. *Journal of Renewable and Sustainable Energy* **2015**, *7*.

[17] Narayan, M. R. Review: Dye sensitized solar cells based on natural photosensitizers. *Renewable and Sustainable Energy Reviews* **2012**, *16*, 208–215.

[18] Semalti, P.; Sharma, S. N. Dye Sensitized Solar Cells (DSSCs) Electrolytes and Natural Photo-Sensitizers: A Review. *Journal of Nanoscience and Nanotechnology* **2019**, *20*, 3647–3658.

[19] Vasco, C.; Riihinen, K.; Ruales, J.; Kamal-Eldin, A. Chemical composition and phenolic compound profile of mortiño (Vaccinium floribundum Kunth). *Journal of Agricultural and Food Chemistry* **2009**, *57*, 8274–8281.

[20] Ramirez-Perez, J.; Maria, C.; Santacruz, C. P. Impact of solvents on the extraction and purification of vegetable dyes onto the efficiency for dye-sensitized solar cells. *Renewables: Wind, Water, and Solar* **2019**, *6*, 1–15.

[21] Suhaimi, S.; Shahimin, M. M. Effect of varied extracting solvent on stability and reliability of DSSCs using natural dyes as photosensitizer. *2014 IEEE Student Conference on Research and Development, SCOReD 2014* **2014**,

[22] NREL, Reference Air Mass 1.5 Spectra. `https://www.nrel.gov/grid/solar-resource/spectra-am1.5.html`.

[23] Riordan, C.; Hulstron, R. What is an air mass 1.5 spectrum?(solar cell performance calculations). **1990**, 1085–1088.

[24] Maultzsch, J. Vibrational properties of carbon nanotubes and graphite. **2004**,

[25] Maultzsch, J.; Reich, S.; Thomsen, C. *Physical Review B - Condensed Matter and Materials Physics*; 2002; Vol. 65; pp 1–4.

[26] Dresselhaus, G.; Dresselhaus, M. S.; Saito, R. *Physical properties of carbon nanotubes*; World scientific, 1998.

[27] Yu, M.-F.; Lourie, O.; Dyer, M. J.; Moloni, K.; Kelly, T. F.; Ruoff, R. S. Strength and breaking mechanism of multiwalled carbon nanotubes under tensile load. *Science* **2000**, *287*, 637–640.

[28] Kim, P.; Shi, L.; Majumdar, A.; McEuen, P. L. Thermal transport measurements of individual multiwalled nanotubes. *Physical review letters* **2001**, *87*, 215502.

[29] Saito, R.; Fujita, M.; Dresselhaus, G.; Dresselhaus, M. S. Electronic structure of graphene tubules based on C 60. *Physical Review B* **1992**, *46*, 1804.

[30] Mei, X.; Jen Cho, S.; Fan, B.; Ouyang, J. High-performance dye-sensitized solar cells with gel-coated binder-free carbon nanotube films as counter electrode. *Nanotechnology* **2010**, *21*.

[31] Nam, J. G.; Park, Y. J.; Kim, B. S.; Lee, J. S. Enhancement of the efficiency of dye-sensitized solar cell by utilizing carbon nanotube counter electrode. *Scripta Materialia* **2010**, *62*, 148–150.

[32] Mei, X.; Ouyang, J. Gels of carbon nanotubes and a nonionic surfactant prepared by mechanical grinding. *Carbon* **2010**, *48*, 293–299.

[33] Fukushima, T.; Kosaka, A.; Ishimura, Y.; Yamamoto, T.; Takigawa, T.; Ishii, N.; Aida, T. Molecular ordering of organic molten salts triggered by single-walled carbon nanotubes. *Science* **2003**, *300*, 2072–2074.

[34] Fukushima, T.; Aida, T. Ionic liquids for soft functional materials with carbon nanotubes. *Chemistry– A European Journal* **2007**, *13*, 5048–5058.

[35] others,, *et al.* A review on the visible light active titanium dioxide photocatalysts for environmental applications. *Applied Catalysis B: Environmental* **2012**, *125*, 331–349.

[36] Mehra, S.; Bishnoi, S.; Jaiswal, A.; Jagadeeswararao, M.; Srivastava, A. K.; Sharma, S. N.; Vashishtha, P. A review on spectral converting nanomaterials as a photoanode layer in dye-sensitized solar cells with implementation in energy storage devices. *Energy Storage* **2020**, *2*, 1–28.

[37] Kang, X.; Liu, S.; Dai, Z.; He, Y.; Song, X.; Tan, Z. Titanium dioxide: from engineering to applications. *Catalysts* **2019**, *9*, 191.

[38] Aboulouard, A.; Gultekin, B.; Can, M.; Erol, M.; Jouaiti, A.; Elhadadi, B.; Zafer, C.; Demic, S. Dye sensitized solar cells based on titanium dioxide nanoparticles synthesized by flame spray pyrolysis and hydrothermal sol-gel methods: a comparative study on photovoltaic performances. *Journal of Materials Research and Technology* **2020**, *9*, 1569–1577.

[39] Xiao, J.; Peng, T.; Li, R.; Peng, Z.; Yan, C. Preparation, phase transformation and photocatalytic activities of cerium-doped mesoporous titania nanoparticles. *Journal of Solid State Chemistry* **2006**, *179*, 1161–1170.

[40] Lee, J. G.; Cheon, J. H.; Yang, H. S.; Lee, D. K.; Kim, J. H. Enhancement of photovoltaic performance in dye-sensitized solar cells with the spin-coated TiO2 blocking layer. *Journal of nanoscience and nanotechnology* **2012**, *12*, 6026–6030.

[41] Perkampus, H.-H. *UV-VIS Spectroscopy and its Applications*; Springer Science & Business Media, 2013.

[42] Munjanja, B.; Sanganyado, E. UV-Visible Absorption, Fluorescence, and Chemiluminescence Spectroscopy. *Handbook of Food Analysis; Nollet, LM, Fidel, T., Eds* **2015**, 572–583.

[43] Calogero, G.; Yum, J. H.; Sinopoli, A.; Di Marco, G.; Grätzel, M.; Nazeeruddin, M. K. Anthocyanins and betalains as light-harvesting pigments for dye-sensitized solar cells. *Solar Energy* **2012**, *86*, 1563–1575.

[44] Campos, R. E.; Sako, E. Y.; dos Reis, M. V. G.; Villalva, M. G. A Review of the Main Methods to trace the IV Characteristic Curve of PV Sources. 2018.

[45] Cáceres, M.; Firman, A.; Montes-Romero, J.; González Mayans, A. R.; Vera, L. H.; F Fernández, E.; de la Casa Higueras, J. Low-Cost I–V Tracer for PV Modules under Real Operating Conditions. *Energies* **2020**, *13*, 4320.

[46] Duran, E.; Piliougine, M.; Sidrach-de Cardona, M.; Galan, J.; Andujar, J. Different methods to obtain the I–V curve of PV modules: A review. 2008.

[47] Titus, D.; Samuel, E. J. J.; Roopan, S. M. *Green Synthesis, Characterization and Applications of Nanoparticles*; Elsevier, 2019; pp 303–319.

[48] Smith, E.; Dent, G. Modern Raman spectroscopy: a practical approach. **2005**,

[49] Saito, R.; Hofmann, M.; Dresselhaus, G.; Jorio, A.; Dresselhaus, M. S. Raman spectroscopy of graphene and carbon nanotubes. *Advances in Physics* **2011**, *60*, 413–550.

[50] Dresselhaus, M. S.; Jorio, A.; Hofmann, M.; Dresselhaus, G.; Saito, R. Perspectives on carbon nanotubes and graphene Raman spectroscopy. *Nano letters* **2010**, *10*, 751–758.

[51] Dresselhaus, M.; Dresselhaus, G.; Jorio, A. Raman spectroscopy of carbon nanotubes in 1997 and 2007. *The Journal of Physical Chemistry C* **2007**, *111*, 17887–17893.

[52] Zhang, B.; Wang, D.; Yu, B.; Zhou, F.; Liu, W. Candle soot as a supercapacitor electrode material. *RSC Advances* **2014**, *4*, 2586–2589.

[53] Bunaciu, A. A.; UdriŞTioiu, E. G.; Aboul-Enein, H. Y. X-ray diffraction: instrumentation and applications. *Critical reviews in analytical chemistry* **2015**, *45*, 289–299.

[54] Patel, J. P.; Parsania, P. H. Characterization, testing, and reinforcing materials of biodegradable composites. *Biodegradable and Biocompatible Polymer Composites; Elsevier: Amsterdam, The Netherlands* **2018**, 55–79.

[55] Rabiei, M.; Palevicius, A.; Monshi, A.; Nasiri, S.; Vilkauskas, A.; Janusas, G. Comparing methods for calculating nano crystal size of natural hydroxyapatite using X-Ray diffraction. *Nanomaterials* **2020**, *10*, 1627.

[56] Meen, T.; Water, W.; Chen, W.; Chao, S.; Ji, L.; Huang, C. Application of TiO2 nano-particles on the electrode of dye-sensitized solar cells. *Journal of Physics and Chemistry of Solids* **2009**, *70*, 472–476.

[57] Kober, T.; Schiffer, H.-W.; Densing, M.; Panos, E. Global energy perspectives to 2060–WEC's World Energy Scenarios 2019. *Energy Strategy Reviews* **2020**, *31*, 100523.

[58] Gong, J.; Sumathy, K.; Qiao, Q.; Zhou, Z. Review on dye-sensitized solar cells (DSSCs): Advanced techniques and research trends. *Renewable and Sustainable Energy Reviews* **2017**, *68*, 234–246.

[59] Ma, J.; Li, C.; Yu, F.; Chen, J. 3 D Single-Walled Carbon Nanotube/Graphene Aerogels as Pt-Free Transparent Counter Electrodes for High Efficiency Dye-Sensitized Solar Cells. *ChemSusChem* **2014**, *7*, 3304–3311.

[60] Sivakumar, V.; Vijaeeswarri, J.; Anna, J. L. Effective natural dye extraction from different plant materials using ultrasound. *Industrial Crops and Products* **2011**, *33*, 116–122.

[61] Ilić, S.; Paunović, V. Characteristics of curcumin dye used as a sensitizer in dye-sensitized solar cells. *Facta universitatis-series: Electronics and Energetics* **2019**, *32*, 91–104.

[62] Rossi, J. E.; Soule, K. J.; Cleveland, E.; Schmucker, S. W.; Cress, C. D.; Cox, N. D.; Merrill, A.; Landi, B. J. Removal of sodium dodecyl sulfate surfactant from aqueous dispersions of single-wall carbon nanotubes. *Journal of Colloid and Interface Science* **2017**, *495*, 140–148.

[63] Mulay, M. R.; Chauhan, A.; Patel, S.; Balakrishnan, V.; Halder, A.; Vaish, R. Candle soot: Journey from a pollutant to a functional material. *Carbon* **2019**, *144*, 684–712.

[64] Thomas, S.; Thomas, R.; Zachariah, A. K.; Kumar, R. *Spectroscopic Methods for Nanomaterials Characterization*; Elsevier, 2017; Vol. 2.

[65] Artur, C. G. Fundamental Investigations into Single Molecule Surface Enhanced Raman Spectroscopy. **2014**,

[66] König, U.; Angélica, R. S.; Norberg, N.; Gobbo, L. Rapid X-ray diffraction (XRD) for grade control of bauxites. *ICSOBA Proceedings* **2012**, *19*, 11pp.

[67] Stoecker, W.; Starbuck, J. Effect of Soller Slits on X-Ray Intensity in a Modern Diffractometer. *Review of Scientific Instruments* **1965**, *36*, 1593–1598.

[68] Yazie, N.; Delele, A.; Ayele, W.; Tsigie, Y. A. Recent advances in anthocyanin dyes extracted from plants for dye sensitized solar cell. *Materials for Renewable and Sustainable Energy* **2020**, *9*, 1–16.

[69] Calogero, G.; Bartolotta, A.; Di Marco, G.; Di Carlo, A.; Bonaccorso, F. Vegetable-based dye-sensitized solar cells. *Chemical Society Reviews* **2015**, *44*, 3244–3294.

[70] Jorio, A.; Saito, R. Raman spectroscopy for carbon nanotube applications. *Journal of Applied Physics* **2021**, *129*, 021102.

[71] Grace, T.; Yu, L.; Gibson, C.; Tune, D.; Alturaif, H.; Othman, Z. A.; Shapter, J. Investigating the effect of carbon nanotube diameter and wall number in carbon nanotube/silicon heterojunction solar cells. *Nanomaterials* **2016**, *6*, 5–9.

[72] Molina-Duarte, J.; Espinosa-Vega, L. I.; Rodríguez, A. G.; Guirado-López, R. A. Raman spectra of single walled carbon nanotubes at high temperatures: Pretreating samples in a nitrogen atmosphere improves their thermal stability in air. *Physical Chemistry Chemical Physics* **2017**, *19*, 7215–7227.

[73] Heller, D. A.; Barone, P. W.; Swanson, J. P.; Mayrhofer, R. M.; Strano, M. S. Using Raman spectroscopy to elucidate the aggregation state of single-walled carbon nanotubes. *The Journal of Physical Chemistry B* **2004**, *108*, 6905–6909.

[74] Fan, B.; Mei, X.; Sun, K.; Ouyang, J. Conducting polymer/carbon nanotube composite as counter electrode of dye-sensitized solar cells. *Applied Physics Letters* **2008**, *93*, 143103.

[75] Maultzsch, J.; Telg, H.; Reich, S.; Thomsen, C. Radial breathing mode of single-walled carbon nanotubes: Optical transition energies and chiral-index assignment. *Physical Review B - Condensed Matter and Materials Physics* **2005**, *72*, 1–16.

[76] Strano, M. S.; Doorn, S. K.; Haroz, E. H.; Kittrell, C.; Hauge, R. H.; Smalley, R. E. Assignment of (n, m) Raman and optical features of metallic single-walled carbon nanotubes. *Nano Letters* **2003**, *3*, 1091–1096.

[77] Fantini, C.; Jorio, A.; Souza, M.; Strano, M.; Dresselhaus, M.; Pimenta, M. Optical transition energies for carbon nanotubes from resonant Raman spectroscopy: Environment and temperature effects. *Physical review letters* **2004**, *93*, 147406.

[78] Cardenas, J. F.; Gromov, A. The effect of bundling on the G Raman band of single-walled carbon nanotubes. *Nanotechnology* **2009**, *20*, 465703.

[79] Cardenas, J. F.; Glerup, M. The influence of surfactants on the distribution of the radial breathing modes of single walled carbon nanotubes. *Nanotechnology* **2006**, *17*, 5212.

[80] Izard, N.; Riehl, D.; Anglaret, E. Exfoliation of single-wall carbon nanotubes in aqueous surfactant suspensions: A Raman study. *Physical Review B* **2005**, *71*, 195417.

[81] Qahtan, T. F.; Gondal, M. A.; Alade, I. O.; Dastageer, M. A. Fabrication of water jet resistant and thermally stable superhydrophobic surfaces by spray coating of candle soot dispersion. *Scientific reports* **2017**, *7*, 1–7.

[82] Sadezky, A.; Muckenhuber, H.; Grothe, H.; Niessner, R.; Pöschl, U. Raman microspectroscopy of soot and related carbonaceous materials: spectral analysis and structural information. *Carbon* **2005**, *43*, 1731–1742.

[83] Gangadharan, A.; Mamidi, S.; Sharma, C. S.; Rao, T. N. Urea-modified candle soot for enhanced anodic performance for fast-charging lithium-ion battery application. *Materials Today Communications* **2020**, *23*, 100926.

[84] Kakunuri, M.; Sharma, C. S. Candle soot derived fractal-like carbon nanoparticles network as high-rate lithium ion battery anode material. *Electrochimica Acta* **2015**, *180*, 353–359.

[85] others,, *et al.* Joint committee on powder diffraction standards. *ASTM, Philadelphia, Pa* **1967**, 9–185.

[86] Al-Alwani, M. A.; Mohamad, A. B.; Kadhum, A. A. H.; Ludin, N. A. Effect of solvents on the extraction of natural pigments and adsorption onto TiO2 for dye-sensitized solar cell applications. *Spectrochimica Acta Part A: Molecular and Biomolecular Spectroscopy* **2015**, *138*, 130–137.

[87] Mansa, R. F.; Govindasamy, G.; Farm, Y. Y.; Bakar, H. A.; Dayou, J.; Sipaut, C. S. Hibiscus flower extract as a natural dye sensitiser for a dye-sensitised solar cell. *Journal of Physical Science* **2014**, *25*, 85.

[88] Hossain, M. K.; Pervez, M. F.; Mia, M.; Mortuza, A.; Rahaman, M.; Karim, M.; Islam, J. M.; Ahmed, F.; Khan, M. A. Effect of dye extracting solvents and sensitization time on photovoltaic performance of natural dye sensitized solar cells. *Results in physics* **2017**, *7*, 1516–1523.